TYPE Original Research
PUBLISHED 30 June 2025
DOI 10.3389/feart.2025.1597623

OPEN ACCESS

EDITED BY
Hu Li,
Sichuan University of Science and Engineering, China

REVIEWED BY
Fangbin Liu,
Qilu Normal University, China
Xin Zhang,
Ningxia University, China

*CORRESPONDENCE
Xinwei Zhai,
zhaixw926@lzu.edu.cn

RECEIVED 21 March 2025
ACCEPTED 16 June 2025
PUBLISHED 30 June 2025

CITATION
Zheng F, Zhai X, Guo Z, Wang E and Wang H (2025) Geochemical characteristics and petrogenetic process of late cretaceous granites in the southern Tibet Gangdese Tectonic Belt.
Front. Earth Sci. 13:1597623.
doi: 10.3389/feart.2025.1597623

Geochemical characteristics and petrogenetic process of late cretaceous granites in the southern Tibet Gangdese Tectonic Belt

Feifei Zheng[1], Xinwei Zhai[1]*, Zhiang Guo[2], Erteng Wang[1] and Haidong Wang[1]

[1]School of Earth Sciences, Key Laboratory of Mineral Resources in Western China (Gansu Province), Lanzhou University, Lanzhou, China, [2]The Senior School Affiliated to Chengdu Institute of Education Science (Sichuan Province), The Senior School of Education Science, Chengdu, China

Introduction: The Gangdese Tectonic Belt was formed through the prolonged subduction and collisional processes involving the Neo-Tethys Ocean and the Indian and Asian continental plates, preserving tectonic evolutionary imprints of both oceanic subduction and continental collision. However, the geodynamic mechanisms controlling Late Cretaceous magmatism in the Gangdese Tectonic Belt remain debated, necessitating further investigation into its magmatic evolution and geodynamic processes.

Methods: This study employs zircon U-Pb geochronology and geochemical analysis (including major, trace element, and Sr-Nd isotope data) on the Xietongmen granite and Longger granite from the Gangdese Tectonic Belt.

Results: The Xietongmen granite formed at 96 Ma, while the Longger granite formed slightly later at 80 Ma. The Xietongmen granite can be classified as a high-K calc-alkaline and weakly peraluminous granite. Geochemically, it is enriched in Sr, depleted in Y, and exhibits high Sr/Y and $(La/Yb)_N$ ratios, displaying geochemical signatures comparable to adakite-like rocks. The Longger granite is a metaluminous granitoid of the high-K calc-alkaline series. Furthermore, the negative correlation of P_2O_5 with SiO_2 and the presence of hornblende and biotite indicate that it belongs to the I-type granites. The Xietongmen and Longger granites were probably derived from the partial melting of the lower crust. The source of the Xietongmen granite may contain residual garnet and hornblende, while the Longger granite likely underwent plagioclase fractional crystallization. The initial $(^{87}Sr/^{86}Sr)_i$ ratios and εNd(t) values (2.78–3.76) of the Xietongmen granite may suggest derivation from a juvenile crustal source.

Discussion: Integrating the data of this study with previous research, the Xietongmen granite was likely formed due to Neo-Tethyan oceanic ridge subduction. In contrast, the Longger granite was formed during the slab rollback phase following ridge subduction.

KEYWORDS

granitoid, Late Cretaceous, petrogenesis, tectonics, Gangdese Tectonic Belt, Neo-Tethys Ocean

1 Introduction

Situated in the southwestern region of China, the Tibetan Plateau represents the highest and youngest plateau on the planet, often referred to as the "Roof of the World" (Yin and Harrison, 2000; Chung et al., 2003; Chung et al., 2005; Hou et al., 2013; Hou et al., 2015; Kapp et al., 2005; Kapp et al., 2007; Ji et al., 2009; Ji et al., 2014; Lee et al., 2012; Xu et al., 2015; Zhu et al., 2013; Ding et al., 2014; Wang et al., 2014; Gibbons et al., 2015). It records the sequential opening and closure of multiple oceanic basins within the Tethyan tectonic domain during the Phanerozoic, preserving intricate geological records of multi-stage subduction, collision, and orogenic processes (Zhang et al., 2012; Ingalls et al., 2016; Webb et al., 2017; van Hinsbergen et al., 2019; Qasim et al., 2018; Baral et al., 2019; Rowley, 2019; Tang et al., 2023; Zhu et al., 2023).

The Gangdese Tectonic Belt (GTB) in the southern Tibetan Plateau is one of the most intensely deformed orogenic belts due to complex tectonic-magmatic interactions and crust-mantle processes. Its formation records the evolutionary history of the Neo-Tethys Ocean (Zhu et al., 2013; Ding et al., 2014; Wang et al., 2014; Wang et al., 2016; Ma et al., 2019), preserving extensive geological evidence of the subduction and closure of the Neo-Tethyan Ocean, the continental collision between the Indian and Eurasian plates, and post-collisional magmatic activities (Wen et al., 2008a; Wen et al., 2008b; Ji et al., 2009; 2014; Zhu et al., 2011; Zhu et al., 2018; Xu et al., 2020). Therefore, investigations of the magmatic rocks within the Gangdese Tectonic Belt provide critical constraints for deciphering the formation and evolution of the Neo-Tethys Ocean and the underlying geodynamic mechanisms driving plateau uplift.

The GTB predominantly comprises magmatic rocks formed since the Late Cretaceous (Wen et al., 2008a; Wen et al., 2008b; Ji et al., 2009; Ji et al., 2014). Studies indicate that the Late Cretaceous represents a critical period for transforming subduction mechanisms in the Neo-Tethyan Ocean. This tectonic process induced regional large-scale magmatic activity, leading to the widespread outcropping of Late Cretaceous magmatic rocks in the Gangdese tectonic belt. Magmatic rocks of this period are predominantly intrusive and dominated by diorite and granodiorite (Ji et al., 2009; Ji et al., 2014; Ma et al., 2013a; Ma et al., 2013b; Zhang S et al., 2014; Xu et al., 2015). However, the deep dynamic mechanisms for the genesis of Late Cretaceous rocks in the Gangdese tectonic belt remain controversial, with three main models proposed: (1) flat-slab subduction of the Neo-Tethyan Ocean (Wen et al., 2008a; Wen et al., 2008b); (2) slab rollback of the Neo-Tethyan Ocean (Ma et al., 2013b); and (3) subduction of the Neo-Tethyan *mid-ocean ridge* (Zhang et al., 2010; Zheng et al., 2014). Each model has a certain degree of validity but requires further geological evidence for validation. Therefore, the complexity of the formation mechanisms of Late Cretaceous magmatic rocks in the Gangdese tectonic belt warrants more in-depth investigation and discussion.

To advance our understanding of the current debate, this study presents zircon U-Pb geochronological data, whole-rock major and trace element compositions, and Sr-Nd isotope data for the Late Cretaceous granites in the central and western segments of the GTB, Tibetan Plateau. Combined with previous research results, we systematically discuss the petrogenesis of these granites and their tectonic settings. The results provide new petrological insights into the formation and evolution of the Neo-Tethys Ocean during the Late Cretaceous in the GTB.

2 Geological setting

Tectonically, the Tibetan Plateau is composed of four major blocks arranged from south to north: the Himalayan block, the Lhasa block, the Qiangtang block, and the Songpan-Ganzi block, with their boundaries delineated by the Indus-Yarlung Zangbo Suture Zone (IYZSZ), the Bangong-Nujiang Suture Zone (BNSZ), and the Jinsha River Suture Zone (JSSZ) (Schärer et al., 1984; Yin and Harrison, 2000; Chu et al., 2006; Guo et al., 2011; Zhu et al., 2011; Zhu et al., 2013). The Gangdese Tectonic Belt, corresponding to the Lhasa terrane, is situated between the BNSZ and the IYZSZ, extending east-west (Yin and Harrison, 2000; Zhu et al., 2011). This belt is characterized by extensive magmatic activity (Figure 1A), forming a vast tectonic-magmatic belt. Throughout its evolution, the GTB has preserved geological records associated with its formation and evolutionary history (Ji et al., 2009; Ran et al., 2019; Zhu et al., 2017; Collins et al., 2020; DePaolo et al., 2019; Ducea et al., 2021). As such, it serves as a natural laboratory for investigating the subduction and collisional dynamics of the Neo-Tethys Ocean.

Notable volcanic sequences exposed within the Gangdese tectono-magmatic belt include the Early to Middle Jurassic Yeba Group volcanic rocks (Zhu et al., 2008), the Late Jurassic to Early Cretaceous Sangri Group volcanic rocks (Zhu et al., 2009a; Kang et al., 2014), and the Early Cretaceous Zenong and Duoni Group volcanic rocks (Figure 1B). Intrusive rocks within the Gangdese tectonic belt include minor gabbro, dolerite, monzodiorite, and abundant granodiorite and granite (Ji et al., 2009; Ji et al., 2014; Ma et al., 2013a; Ma et al., 2013b), with Late Cretaceous plutonic rocks exhibiting the greatest lithological diversity and the most extensive exposure.

3 Petrography

The Xietongmen granite is grayish-white, exhibiting a porphyaceous texture and massive structure. The dominant phenocrysts include quartz and plagioclase, while the matrix consists of microcrystalline plagioclase and quartz (Figures 2A–C). The quartz phenocrysts are primarily euhedral to subhedral, with grain sizes varying between 5 and 7 mm, constituting 30%–35% of the total composition. The plagioclase phenocrysts exhibit moderate alteration, undergoing sericitization, constituting roughly 25%–30% of the rock. The groundmass constitutes 25%–30% of the rock, with minor amounts of strongly altered biotite, constituting approximately 5%.

The Longger granite is also grayish-white, displaying a medium-to-fine-grained structure with a homogeneous texture (Figures 2D–F). Its primary mineral constituents include microperthite (30%–35%), plagioclase (30%–35%), quartz (15%–20%), biotite (~5%), and a minor proportion of hornblende (~5%). Common accessory minerals include zircon, apatite, and

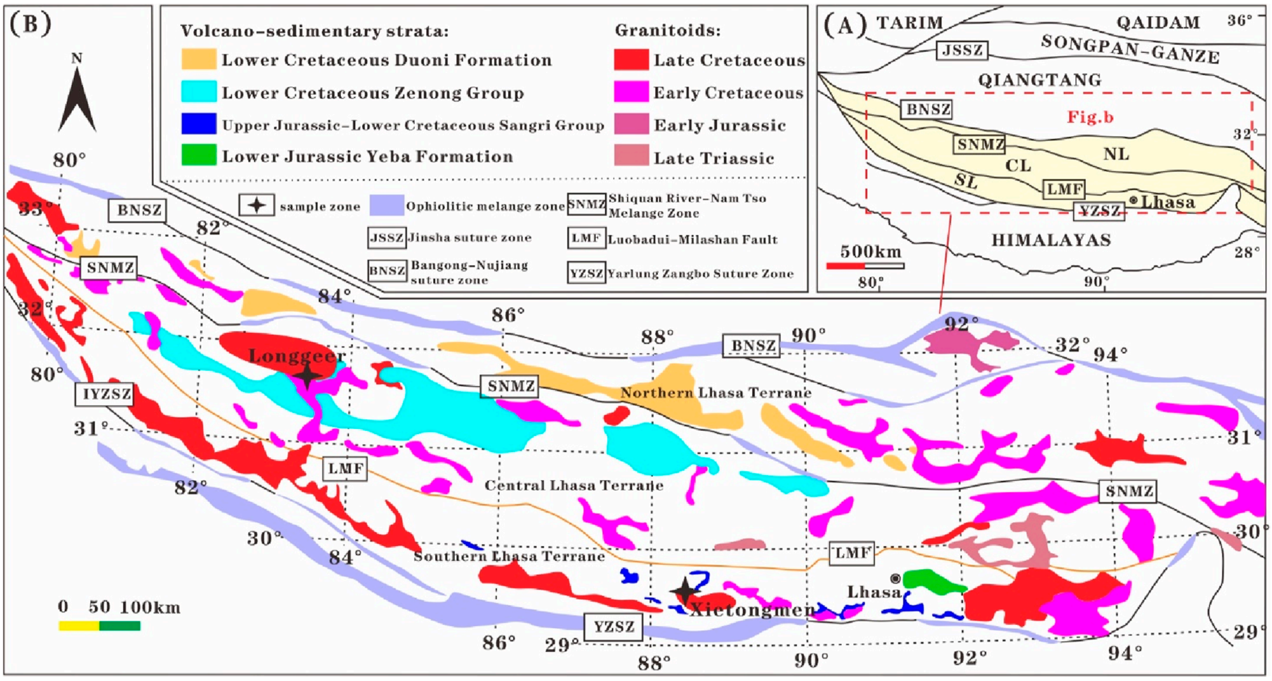

FIGURE 1
(A) Tectonic structure of the Tibetan Plateau. **(B)** Spatial distribution of the Gangdese magmatic belt with sample locations. [**(A,B)** modified after Zhu et al., 2011].

iron-rich opaque phases such as magnetite. Microperthite occurs as subhedral to anhedral columnar grains, exhibiting distinct grid twinning. Plagioclase appears as euhedral to subhedral columnar grains, showing well-developed polysynthetic twinning. Quartz is smoky gray, predominantly subhedral to anhedral, having a grain size ranging from 0.2 to 0.5 mm. Biotite forms anhedral flakes, commonly distributed along the margins of other minerals, with evident chloritization. Hornblende is brown, euhedral to subhedral, and is characterized by two sets of inclined cleavages forming an angle of approximately 56°.

4 Analytical methods

Nanjing Hongchuang Geological Exploration Technology Service Co., Ltd. Conducted zircon selection, target preparation, and whole-rock Sr-Nd isotopic analysis. U-Pb isotopic dating of zircons and major and trace element analyses of whole-rock samples were performed at the Key Laboratory of Mineral Resources in Western China, Lanzhou University.

4.1 Zircon U-Pb dating

Initially, the rock samples underwent crushing and washing, and then electromagnetic and heavy liquid separation were applied to concentrate zircon grains. Using a binocular microscope, a selection of well-shaped, larger zircon grains was made and then set in epoxy resin, followed by polishing to prepare analytical mounts. For these polished zircon grains, the most suitable candidates—those exhibiting clear internal zoning without noticeable cracks or bubbles—were selected based on cathodoluminescence (CL), transmission, and reflection imaging. These zircons were then analyzed using laser ablation inductively coupled plasma mass spectrometry (LA-ICP-MS) on an Agilent 7500a ICP-MS system, using a 30 μm laser spot diameter with He as the carrier gas. The reference standards NIST 91500 and NIST 610 were employed for instrumental calibration. Finally, data processing and plotting were conducted using the Glitter and Isoplot software packages.

4.2 Whole-rock geochemical analysis

Major element concentrations were determined using a Leeman Prodigy inductively coupled plasma optical emission spectrometer (ICP-OES). Before analysis, the samples were cleaned, dried, and powdered, then subjected to high-temperature ignition at 1,000°C for 2 h in a crucible. The mass difference before and after heating was recorded to calculate the loss on ignition (LOI). The samples were subsequently fused with lithium metaborate ($LiBO_2$), and the resulting solutions were transferred into volumetric flasks, diluted to a predetermined volume, and weighed for subsequent analysis. For trace element analysis, a high-temperature and high-pressure closed digestion method was employed for sample preparation, followed by analysis using an Agilent 7,700X inductively coupled plasma mass spectrometer (ICP-MS). Whole-rock Sr-Nd isotopic measurements were performed using a Nu Instruments Nu Plasma II MC–ICP–MS

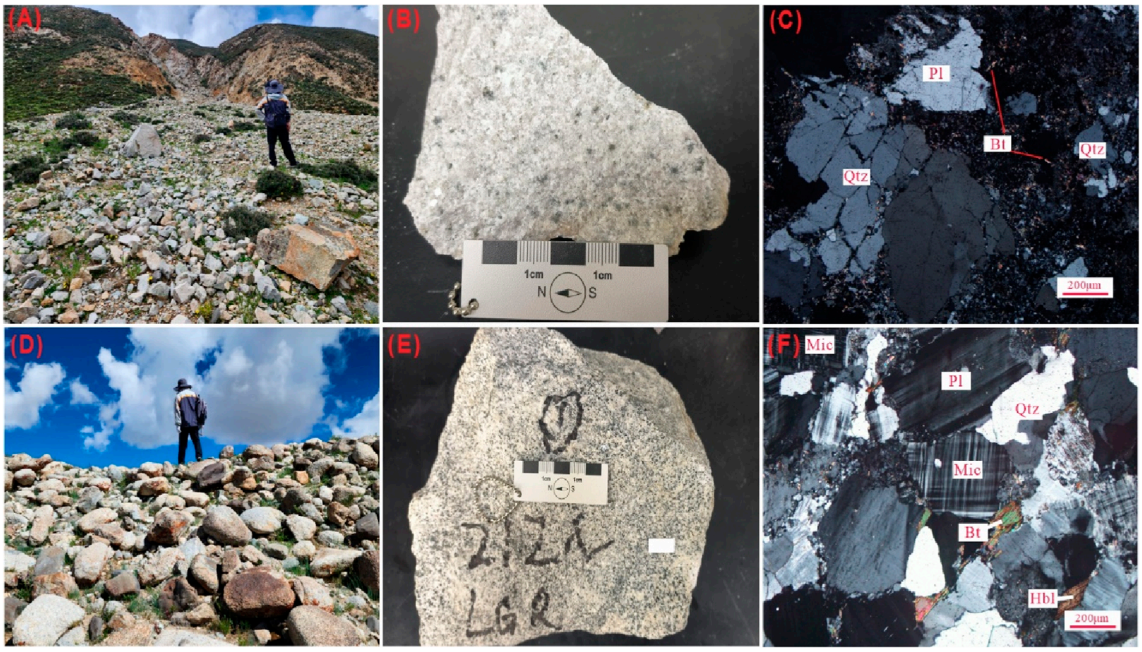

FIGURE 2
Field outcrops, hand-specimen photographs, and microphotographs of Late Cretaceous magmatic rocks from the Xietongmen area **(A–C)** and the Longger area **(D–F)**. Abbreviation: Qtz, Quartz; Pl, plagioclase; Kfs, K-feldspar; Mic, microperthite; Hbl, hornblende; Bt, biotite.

device. BCR-2 and AGV-2 were used as external standards, while GSB was employed to monitor Nd isotope measurements.

5 Results

5.1 Zircon U-Pb ages

The zircon U-Pb dating results for the samples from the Xietongmen and Longger granites are presented in Table 1.

The zircon grains extracted from the Xietongmen granite are highly euhedral and predominantly prismatic, with grain sizes ranging from 30 to 150 μm and aspect ratios of 1:1 to 3:1. They show clear magmatic oscillatory zoning in the Cathodoluminescence (CL) images (Figure 3A). The Th/U ratios range from 0.67 to 1.27, aligning with the characteristics of magmatic zircons (Hoskin and Ireland, 2000). Among the 20 zircon spots analyzed for U-Pb isotopes, spots 3 (103 ± 1 Ma) and 8 (107 ± 1 Ma) yielded older ages, suggesting that they are inherited zircons. The remaining 18 zircon spots exhibit a relatively concentrated age distribution on the U-Pb concordia diagram (Figure 4A). The weighted mean $^{206}Pb/^{238}U$ age of these zircons is 95.9 ± 0.6 Ma (MSWD = 1.3), representing the crystallization age of the Xietongmen granite formed in the Late Cretaceous.

Similar to the Xietongmen granite, the Longger granite contains highly euhedral zircon grains, mostly prismatic, with grain sizes ranging from 50 to 150 μm and aspect ratios of 1:1 to 3:1. Their CL images display clear magmatic oscillatory zoning (Figure 3B). The Th/U ratios range from 0.36 to 2.34, consistent with the characteristics of magmatic zircons (Hoskin and Ireland, 2000). Among the 30 zircon spots analyzed, spots 1, 7, 19, and 22 yielded older ages, suggesting that they are inherited zircons. The remaining 26 spots exhibit a relatively concentrated age distribution on the U-Pb concordia diagram (Figure 4B). The weighted mean $^{206}Pb/^{238}U$ age of these zircons is 79.5 ± 0.4 Ma (MSWD = 1.04), representing the crystallization age of the Late Cretaceous Longger granite.

5.2 Major and trace elements

Whole-rock major and trace-element compositions of the Xietongmen and Longger granites are presented in Table 2.

All samples from the Xietongmen granite exhibit comparatively low LOIs (0.92–2.09 wt%). They are characterized by high SiO_2 (68.16–74.17 wt%), Al_2O_3 (12.84–16.24 wt%), K_2O (2.83–4.65 wt%), Na_2O (2.77–4.33 wt%) contents, and low CaO (1.79–2.65 wt%), TiO_2 (0.45–0.60 wt%), P_2O_5 (0.08–0.15 wt%), MgO (0.76–1.34 wt%) contents. The total alkali (Na_2O + K_2O) contents vary between 7.08 wt% and 8.40 wt%, and the Rittmann indices (σ = 1.69–2.73) remain below 3.3.

Longger granite samples have low LOIs (0.23–0.80 wt%), high SiO_2 (66.29–72.58 wt%), K_2O (3.36–6.49 wt%), Na_2O (3.23–4.85 wt%), Al_2O_3 (14.64–16.27 wt%) contents, and low $Fe_2O_3^T$ (0.58–2.88 wt%), MgO (0.17–1.07 wt%, $Mg^{\#}$ = 27.88–47.42) contents. Total alkali contents range from 8.00 to 10.37 wt%, and Rittmann indices vary between 2.49 and 4.11.

In the K_2O + Na_2O versus SiO_2 diagram (Figure 5A), all Xietongmen granite samples plot within the granite field, and most Longger granite samples fall into the quartz monzonite field. In the K_2O versus SiO_2 diagram (Figure 5B), most Xietongmen

TABLE 1 LA-ICP-MS zircon U-Pb analytical date of Xietongmen granite and Longer granite.

Granite type	Point no	Th/U	Isotope ratio						Age (Ma)			
			$^{207}Pb/^{206}Pb$	±1σ	$^{207}Pb/^{235}U$	±1σ	$^{206}Pb/^{238}U$	±1σ	$^{207}Pb/^{235}U$	±1σ	$^{206}Pb/^{238}U$	±1σ
Xietongmen	XTM-01	0.85	0.05345	0.00156	0.09902	0.00300	0.01499	0.00020	96	3	96	1
	XTM-02	0.84	0.04114	0.00124	0.09632	0.00303	0.01532	0.00020	93	3	98	1
	XTM-03	0.70	0.06409	0.00172	0.14076	0.00398	0.01615	0.00020	134	4	103	1
	XTM-04	0.71	0.05270	0.00102	0.10730	0.00225	0.01536	0.00020	103	2	98	1
	XTM-05	0.83	0.04028	0.00082	0.08355	0.00183	0.01485	0.00019	81	2	95	1
	XTM-06	1.00	0.04907	0.0008	0.10495	0.00203	0.01504	0.00020	101	2	96	1
	XTM-07	0.78	0.04637	0.00199	0.09654	0.00394	0.01510	0.00020	94	4	97	1
	XTM-08	0.87	0.07369	0.00132	0.17037	0.00339	0.01669	0.00022	160	3	107	1
	XTM-09	1.27	0.04715	0.00071	0.09968	0.00170	0.01490	0.00019	96	2	95	1
	XTM-10	0.74	0.04812	0.00143	0.10302	0.00320	0.01506	0.00020	100	3	96	1
	XTM-11	1.08	0.05982	0.00089	0.12320	0.00210	0.01499	0.00019	102	2	96	1
	XTM-12	0.75	0.05549	0.00249	0.11218	0.00479	0.01466	0.00020	108	4	94	1
	XTM-13	0.88	0.05733	0.00121	0.11479	0.00262	0.01509	0.00020	110	2	97	1
	XTM-14	1.06	0.04925	0.00082	0.09607	0.00179	0.01470	0.00019	93	2	94	1
	XTM-15	0.96	0.06109	0.00308	0.12450	0.00601	0.01478	0.00022	109	5	95	1
	XTM-16	1.05	0.04727	0.00248	0.09686	0.00489	0.01486	0.00021	94	5	95	1
	XTM-17	0.78	0.05940	0.00150	0.12234	0.00329	0.01514	0.00020	107	3	97	1
	XTM-18	0.86	0.03838	0.00142	0.07911	0.00301	0.01496	0.00020	77	3	96	1
	XTM-19	0.75	0.06235	0.00265	0.12850	0.00516	0.01495	0.00021	123	5	96	1
	XTM-20	0.72	0.05403	0.00084	0.11393	0.00202	0.01505	0.00020	110	2	96	1
Longger	LGR-01	1.02	0.05271	0.00208	0.08666	0.00351	0.01352	0.00019	84	3	87	1
	LGR-02	1.21	0.05227	0.00166	0.08094	0.00264	0.01238	0.00016	79	2	79	1
	LGR-03	1.12	0.04727	0.00183	0.08010	0.00315	0.01274	0.00016	78	3	82	1
	LGR-04	1.03	0.05268	0.00065	0.08365	0.00111	0.01218	0.00014	82	1	78	0.9
	LGR-05	0.86	0.04725	0.00239	0.08086	0.00395	0.01241	0.00016	79	4	80	1
	LGR-06	1.27	0.05602	0.0012	0.09003	0.00200	0.01266	0.00015	88	2	81.1	1
	LGR-07	1.59	0.05117	0.00106	0.20523	0.00462	0.02927	0.00036	190	4	186	2
	LGR-08	2.34	0.05699	0.00128	0.09071	0.00211	0.01261	0.00016	88	2	81	1
	LGR-09	1.21	0.04713	0.00077	0.07585	0.00129	0.01240	0.00015	74	1	79.4	1
	LGR-10	1.10	0.05436	0.00101	0.08534	0.00164	0.01253	0.00015	83	2	80.3	1
	LGR-11	1.37	0.05665	0.00136	0.08535	0.00210	0.01234	0.00015	83	2	79.1	1

(Continued on the following page)

TABLE 1 (*Continued*) LA-ICP-MS zircon U-Pb analytical date of Xietongmen granite and Longer granite.

Granite type	Point no	Th/U	Isotope ratio						Age (Ma)			
			$^{207}Pb/^{206}Pb$	±1σ	$^{207}Pb/^{235}U$	±1σ	$^{206}Pb/^{238}U$	±1σ	$^{207}Pb/^{235}U$	±1σ	$^{206}Pb/^{238}U$	±1σ
	LGR-12	1.33	0.05265	0.00073	0.08464	0.00124	0.01244	0.00015	82	1	79.7	1
	LGR-13	1.35	0.04963	0.00109	0.07829	0.00176	0.01226	0.00015	77	2	78.6	1
	LGR-14	2.01	0.05007	0.00102	0.08300	0.00175	0.0126	0.00016	81	2	81	1
	LGR-15	1.94	0.04915	0.00133	0.08098	0.00225	0.01228	0.00016	79	2	79	1
	LGR-16	0.80	0.04816	0.00143	0.08029	0.00244	0.01227	0.00016	78	2	79	1
	LGR-17	1.01	0.05569	0.00092	0.08483	0.00145	0.01263	0.00015	83	1	80.9	1
	LGR-18	1.46	0.05154	0.00117	0.08044	0.00187	0.01226	0.00015	79	2	78.6	1
	LGR-19	1.00	0.05635	0.00089	0.14954	0.00248	0.02252	0.00027	142	2	144	2
	LGR-20	1.46	0.05387	0.00137	0.08062	0.00209	0.01235	0.00016	79	2	79	1
	LGR-21	2.09	0.05236	0.00116	0.07999	0.00182	0.01231	0.00015	78	2	78.9	1
	LGR-22	0.36	0.05513	0.00072	0.12197	0.00166	0.01836	0.00022	117	2	117	1
	LGR-23	2.02	0.06008	0.00116	0.08183	0.00162	0.01230	0.00015	80	2	78.8	1
	LGR-24	1.11	0.05507	0.00107	0.07949	0.00159	0.01243	0.00015	78	1	79.6	1
	LGR-25	1.21	0.06125	0.0012	0.08188	0.00164	0.01234	0.00015	80	2	79.1	1
	LGR-26	1.07	0.06258	0.00237	0.08314	0.00321	0.01254	0.00018	81	3	80	1
	LGR-27	1.28	0.05094	0.00134	0.07841	0.00211	0.01223	0.00016	77	2	78	1
	LGR-28	1.22	0.05588	0.00129	0.08303	0.00196	0.01245	0.00016	81	2	80	1
	LGR-29	1.38	0.05691	0.00126	0.08182	0.00185	0.01228	0.00016	80	2	79	1
	LGR-30	1.22	0.05094	0.00116	0.08289	0.00193	0.01240	0.00016	81	2	79	1

and Longger granites plot within the high-K calc-alkaline field. In the A/NK versus A/CNK diagram (Figure 5C), most Xietongmen samples fall into the weakly peraluminous field, whereas Longger samples are predominantly metaluminous. Thus, the Xietongmen granite exhibits high-K calc-alkaline and weakly peraluminous geochemical characteristics, while the Longger granite is characterized by high-K calc-alkaline and metaluminous characteristics.

Regarding trace elements, the total rare earth element (ΣREE) concentrations of the Xietongmen granite samples range from 16.76 ppm to 128.20 ppm, indicating a low concentration. The light REE to heavy REE (ΣLREE/ΣHREE) ratios vary from 2.43 to 13.88, while the chondrite-normalized $(La/Yb)_N$ ratios range from 2.10 to 16.90, indicating significant enrichment of LREE relative to HREE and notable fractionation between the two rare earth groups.

The Longger granite samples show ΣREE concentrations between 141.72 ppm and 296.98 ppm. The LREE/HREE ratios vary between 5.53 and 27.72, and the $(La/Yb)_N$ values vary between 5.60 and 58.29, showing strong LREE enrichment and fractionation between LREE and HREE.

Both the Xietongmen granite and Longger granite exhibit similar chondrite-normalized rare earth element (REE) patterns (Figures 6A,C), characterized by significant enrichment in LREEs and strong depletion in HREEs, with a rightward-sloping trend in the chondrite-normalized REE pattern. The primitive mantle-normalized multi-element spider (Figures 6B,D) diagram demonstrates that the Xietongmen and Longger granite samples exhibit enrichment in K, Rb, Th, U, and Pb, while showing depletion in Nb, Ta, Ti, and P.

5.3 Sr-Nd isotope systems

Whole-rock Sr–Nd isotopic compositions for the Xietongmen granite samples are listed in Table 3. Based on the granite's crystallization age of 96 Ma, the $^{87}Sr/^{86}Sr$ ratios range from 0.706045 to 0.706255, and initial $^{87}Sr/^{86}Sr$ ratios $[(^{87}Sr/^{86}Sr)_i]$ vary between 0.7042 and 0.7044. The $^{143}Nd/^{144}Nd$ values range

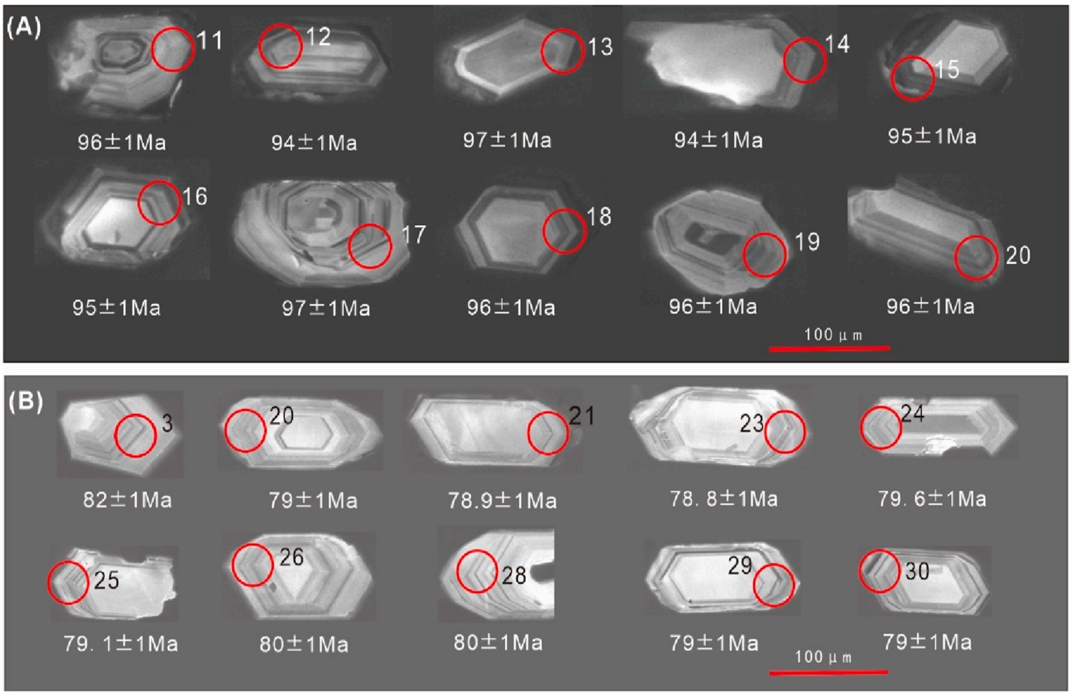

FIGURE 3
Cathodoluminescence (CL) images and U-Pb age (Ma) analysis of representative zircon grains for the Xietongmen granite **(A)** and Longer granite **(B)**.

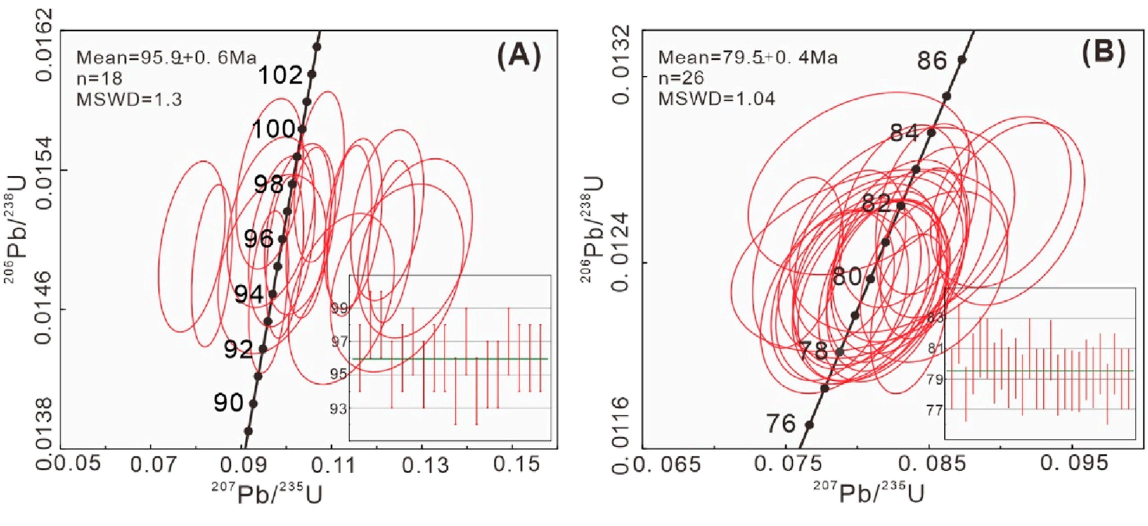

FIGURE 4
Zircon U-Pb concordia diagrams and weighted ages for the Xietongmen granite **(A)** and Longer granite **(B)**.

from 0.512744 to 0.512781, and initial $^{143}Nd/^{144}Nd$ ratios $[(^{143}Nd/^{144}Nd)_i]$ range from 0.512657 to 0.512707. The ε_{Nd} (t = 96 Ma) values vary between +2.78 and +3.76, and all of the samples have relatively young two-stage Nd model ages (T_{DM2}) that vary between 591 and 670 Ma. The five granite samples analyzed exhibit positive $\varepsilon_{Nd}(t)$ values, with a narrow range of variation (within one ε unit), indicating a relatively homogeneous magma source.

6 Discussion

6.1 Petrogenesis of the xietongmen adakite

The Xietongmen granite samples are characterized by high SiO_2 (68.16–74.17 wt%), Al_2O_3 (12.82–16.24 wt%), Sr (226–364 ppm), low MgO (0.76–1.34 wt%), Y (2.93–12.28 ppm), and Yb (0.40–1.47 ppm) contents, and corresponding high Sr/Y

TABLE 2 Whole-rock geochemical data of granites from Xietongmen and Longer regions (major elements: wt%; trace elements: ppm).

Elements	Xietongmen granite						Longer granite				
Sample	XTM-1	XTM-2	XTM-3	XTM-4	XTM-5	XTM-6	LGR-4	LGR-5	LGR-6	LGR-7	LGR-8
SiO_2	69.20	70.57	68.84	68.16	74.17	72.59	72.58	67.93	68.77	66.29	69.16
TiO_2	0.57	0.53	0.60	0.60	0.45	0.56	0.12	0.54	0.37	0.57	0.18
Al_2O_3	16.23	14.38	16.24	15.45	12.84	15.04	14.64	15.79	15.80	16.27	16.07
$Fe_2O_3{}^T$	1.42	2.57	1.56	3.27	0.82	0.87	0.58	2.23	2.35	2.88	1.21
MnO	0.18	0.25	0.26	0.33	0.13	0.11	0.16	0.33	0.46	0.55	0.28
MgO	1.34	0.85	1.24	1.00	0.76	0.79	0.17	0.69	1.07	0.97	0.24
CaO	2.65	2.29	2.21	2.11	1.79	2.41	1.21	2.94	2.80	3.25	1.82
Na_2O	3.88	3.76	2.77	3.86	4.33	4.25	4.14	4.83	3.23	4.85	3.88
K_2O	3.51	3.86	4.65	4.42	4.07	2.83	6.04	4.16	4.77	3.36	6.49
P_2O_5	0.14	0.15	0.14	0.15	0.10	0.08	0.03	0.11	0.06	0.28	0.03
Major contituents (wt%)											
LOI	1.62	1.19	1.48	0.92	2.09	1.25	0.52	0.40	0.38	0.23	0.80
total	100.75	100.39	99.99	100.27	101.54	100.78	100.19	99.95	100.06	99.50	100.16
$Mg^\#$	65.20	39.50	61.19	37.74	64.83	64.32	36.82	38.01	47.42	40.14	27.88
A/NK	1.59	1.39	1.69	1.39	1.11	1.50	1.10	1.27	1.51	1.40	1.20
A/CNK	1.08	0.99	1.19	1.03	0.87	1.04	0.94	0.89	1.01	0.93	0.96
Na_2O/K_2O	1.11	0.97	0.60	0.87	1.06	1.50	0.69	1.16	0.68	1.44	0.60
$Na_2O + K_2O$	7.39	7.62	7.42	8.28	8.40	7.08	10.18	8.99	8.00	8.21	10.37
Rittman indices	2.08	2.10	2.13	2.73	2.26	1.69	3.50	3.24	2.49	2.89	4.11
Trace elements (ppm)											
Sc	5.88	5.46	5.63	6.16	3.97	4.22	5.85	2.53	6.33	3.94	3.91
V	52.91	51.90	55.75	60.26	35.04	36.17	2.88	36.29	42.94	43.16	4.84
Cr	19.09	19.32	20.58	21.16	13.17	16.85	0.95	6.87	14.92	8.55	1.85
Mn	158	210	226	291	109	90.67	125	271	352	446	203
Co	92.14	84.28	104	102	62.03	87.13	127	95.29	97.48	114	85.76
Ni	10.01	7.03	11.22	11.55	5.88	5.53	0.60	3.92	6.79	5.29	0.74
Cu	2.98	1.21	3.27	34.91	1.40	5.49	791.70	1.52	1.08	0.71	5.16
Zn	43.24	35.43	46.54	52.96	42.07	18.22	7.24	45.21	28.82	62.80	13.35
Ga	17.23	18.18	17.40	19.37	11.00	13.31	20.96	29.32	17.87	27.66	20.94
Rb	137	149	177	166	125	130	323	98.42	233	120	253

(Continued on the following page)

TABLE 2 (*Continued*) Whole-rock geochemical data of granites from Xietongmen and Longer regions (major elements: wt%; trace elements: ppm).

Elements	Xietongmen granite						Longer granite				
Sample	XTM-1	XTM-2	XTM-3	XTM-4	XTM-5	XTM-6	LGR-4	LGR-5	LGR-6	LGR-7	LGR-8
Sr	333	302	360	364	226	311	55.83	1,031	146	624	116
Y	6.18	12.28	7.92	11.89	2.93	9.81	42.87	12.16	20.48	10.51	32.25
Zr	96.28	72.70	50.64	61.36	107	53.65	80.84	49.95	85.87	123	111
Nb	9.19	7.96	9.87	9.17	5.57	9.74	21.68	10.73	10.76	8.28	10.45
Mo	0.89	0.34	7.93	0.46	0.50	0.15	0.14	0.24	0.27	0.13	0.21
Cs	10.01	11.58	12.36	10.65	8.17	7.90	3.35	1.67	6.52	3.45	3.12
Ba	446	439	587	531	511	274	158	989	280	391	501
La	7.86	34.65	15.85	26.91	4.10	3.51	34.66	78.20	33.59	47.40	48.38
Ce	12.61	56.99	26.59	44.71	6.81	6.21	64.71	140.23	62.97	91.99	90.19
Pr	1.35	5.64	2.61	4.48	0.69	0.73	6.47	14.23	6.38	9.69	9.20
Nd	4.90	18.57	8.97	14.93	2.49	2.90	21.52	46.32	21.03	33.07	30.90
Sm	0.89	2.99	1.61	2.79	0.48	0.95	4.84	6.33	3.88	4.92	5.79
Eu	0.47	0.74	0.51	0.85	0.25	0.55	0.39	1.33	0.59	0.95	0.78
Gd	0.97	2.44	1.37	2.58	0.47	1.24	5.27	4.31	3.48	3.33	5.86
Tb	0.16	0.37	0.21	0.37	0.08	0.23	0.98	0.52	0.53	0.41	0.94
Dy	0.93	2.12	1.26	2.24	0.46	1.63	6.35	2.60	3.31	2.09	5.55
Ho	0.21	0.45	0.26	0.44	0.10	0.35	1.39	0.46	0.70	0.37	1.12
Er	0.63	1.33	0.77	1.28	0.32	1.12	4.26	1.20	2.15	1.04	3.33
Tm	0.09	0.21	0.12	0.20	0.04	0.17	0.65	0.16	0.33	0.16	0.48
Yb	0.70	1.47	0.78	1.34	0.40	1.20	4.44	0.96	2.40	1.02	3.01
Lu	0.12	0.23	0.12	0.20	0.06	0.17	0.63	0.12	0.36	0.15	0.45
Hf	3.34	2.37	2.02	2.22	3.40	2.11	3.82	1.48	3.32	3.69	4.17
Ta	1.17	1.03	1.20	1.18	0.36	1.17	4.29	0.97	1.84	1.05	0.98
Pb	12.98	6.67	13.80	13.67	8.97	5.01	48.39	20.77	33.09	23.57	47.33
Th	23.04	19.38	38.18	21.12	14.98	18.25	48.99	16.96	39.12	23.72	46.02
U	4.35	4.53	5.24	5.34	2.66	4.03	21.73	1.51	3.93	2.66	4.46
ΣREE	31.90	128.20	61.03	103.31	16.76	20.96	156.56	296.98	141.72	196.60	205.99
ΣLREE	28.09	119.58	56.15	94.67	14.82	14.84	132.59	286.64	128.44	188.02	185.24
ΣHREE	3.81	8.62	4.88	8.64	1.94	6.12	23.98	10.34	13.28	8.58	20.75
LREE/HREE	7.37	13.88	11.50	10.96	7.65	2.43	5.53	27.72	9.67	21.90	8.93

(Continued on the following page)

TABLE 2 (*Continued*) Whole-rock geochemical data of granites from Xietongmen and Longer regions (major elements: wt%; trace elements: ppm).

Elements	Xietongmen granite						Longer granite				
Sample	XTM-1	XTM-2	XTM-3	XTM-4	XTM-5	XTM-6	LGR-4	LGR-5	LGR-6	LGR-7	LGR-8
δEu	1.55	0.84	1.06	0.97	1.60	1.55	0.23	0.78	0.49	0.72	0.41
$(La/Yb)_N$	8.11	16.90	14.55	14.42	7.43	2.10	5.60	58.29	10.04	33.20	11.51
$(Gd/Yb)_N$	1.16	1.37	1.45	1.60	0.98	0.86	0.98	3.71	1.20	2.69	1.61
$(La/Sm)_N$	5.70	7.48	6.34	6.23	5.48	2.39	4.63	7.98	5.59	6.22	5.40

A/CNK = $Al_2O_3/(K_2O + Na_2O + CaO)$ (mole ratio), Mg# = 100 × Mg/(Mg + Fe), $Fe_2O_3{}^T$–total iron reported as Fe_2O_3, δEu = $2Eu_N/(Sm \times Gd)_N$, N denotes chondrite-normalized values, with normalization values based on (Sun and McDonough, 1989).

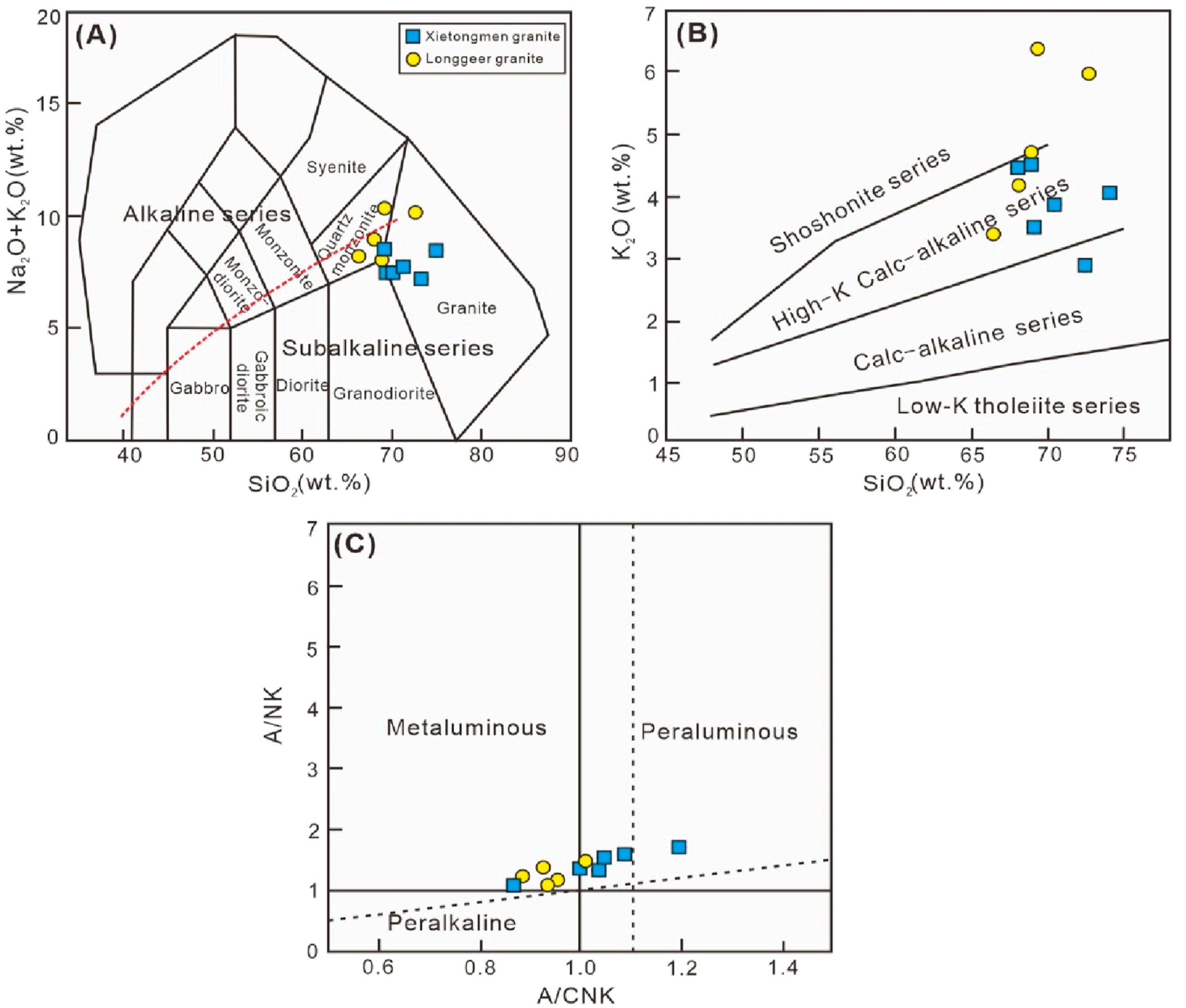

FIGURE 5
Geochemical diagrams of granites in Xietongmen and Longer area **(A)** Total alkali ($Na_2O + K_2O$) versus silica (SiO_2) diagram (Middlemost, 1994); **(B)** K_2O versus SiO_2 diagram (Rickwood, 1989); **(C)** A/NK versus A/CNK diagram (Maniar and Piccoli, 1989).

10.3389/feart.2025.1597623

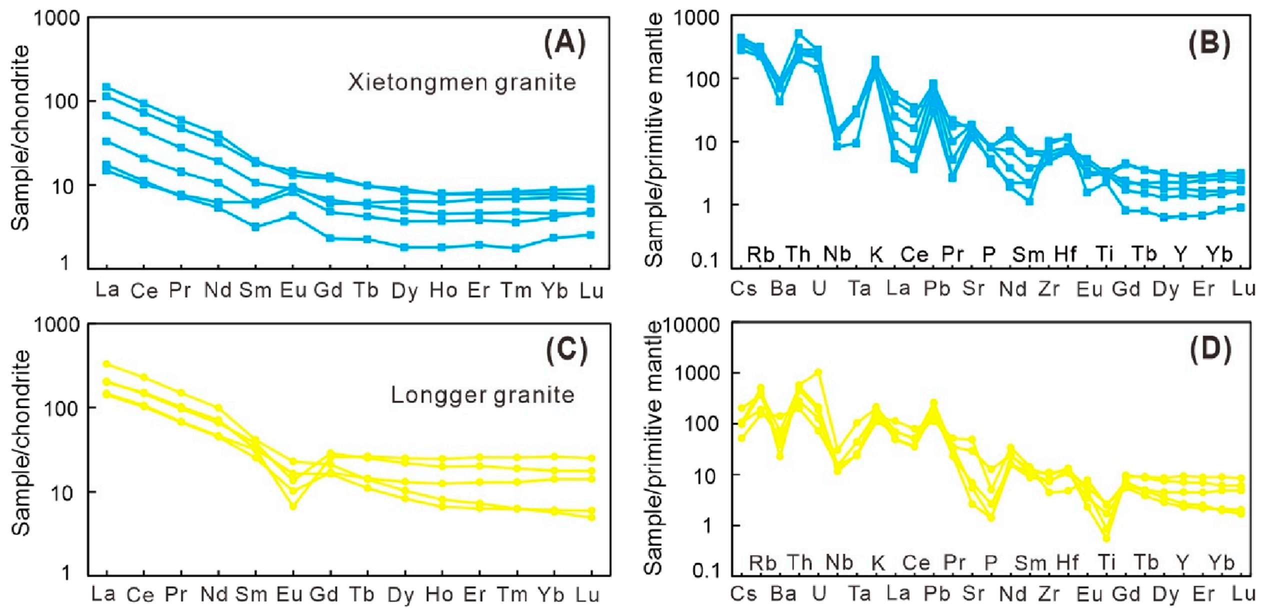

FIGURE 6
The chondrite-normalized rare earth element (REE) patterns **(A,C)** and primitive mantle-normalized trace element spider diagrams **(B,D)** for granites from the Xietongmen and Longger areas, respectively. The normalization values for chondrite and primitive mantle are from Sun and McDonough (1989).

(24.59–77.13) and La/Yb (2.10–16.90) ratios. All samples display LREE enrichment and depletion in HREEs and HFSEs (such as Nb and Ta), with slightly positive Eu anomalies. These geochemical features are comparable to those of adakitic rocks (Defant and Drummond, 1990; Castillo, 2006), which are generally defined by $Al_2O_3 \geq 15$ wt%, MgO ≤3 wt% (rarely exceeding 6 wt%), Y < 18 ppm, Yb ≤ 1.9 ppm, Sr > 400 ppm, Sr/Y > 20, with slightly positive Eu anomalies (Defant and Drummond, 1990; Castillo, 2006).In the Sr/Y versus Y (Figure 7A) and $(La/Yb)_N$ versus Yb_N (Figure 7B) diagrams, the Xietongmen granite samples are positioned within the adakite field, showing that they have an adakitic geochemical signature.

Adakite was initially regarded as derived from the partial melting of a young subducted oceanic slab (Defant and Drummond, 1990). However, recent studies propose several possible formation mechanisms for adakite, as follows: (1) partial melting of subducted oceanic crust (Rapp et al., 1999; Zhu et al., 2009b); (2) partial melting of thickened lower continental crust (Atherton and Petford, 1993; Hou et al., 2013); (3) partial melting of subducted continental crust (Wang et al., 2008); (4) fractional crystallization of primary basaltic magma (Macpherson et al., 2006).

Adakite derived from the fractional crystallization of primary basaltic magma typically leads to a distinct negative Eu anomaly and positive correlations between Sr/Y, Dy/Yb, La/Yb, and SiO_2 (Macpherson et al., 2006). However, the Xietongmen adakitic rock has no such characteristics. In the La versus La/Yb plot (Figure 7C), its geochemical signature is more consistent with partial melting than fractional crystallization. Therefore, the formation of the Xietongmen adakitic rock cannot be attributed to fractional crystallization.

Adakitic rocks formed by partial melting of subducted continental crust typically exhibit higher Th/Ba and Rb/Ba ratios, and negative $\varepsilon_{Nd}(t)$ values (Lai and Qin, 2013). However, Xietongmen adakitic rock samples have low Th/Ba (0.03–0.07), Rb/Ba (0.24–0.48) ratios, and positive $\varepsilon_{Nd}(t)$ values (2.78–3.76). Moreover, the Xietongmen adakitic rock formed at 95.9 Ma during the northward subduction of the Neo-Tethyan oceanic lithosphere beneath the Eurasian continent, rather than during the subduction of continental crust. Therefore, this interpretation is also ruled out.

Adakitic rocks derived from partial melting of a subducted oceanic slab typically have low K_2O content (Defant and Drummond, 1990). The samples of Xietongmen adakitic rock have comparatively high K_2O (2.83–4.65 wt%), similar to the K_2O contents (2.9–4.1 wt%) of adakitic rocks derived from lower crustal melting (Defant and Drummond, 1990). Their Nb/Ta ratios (7.71–15.43) are also close to those of continental crust (11–14) (Taylor and McLennan, 1995). Furthermore, all samples of the Xietongmen adakitic rock have low MgO (0.76–1.34 wt%), Cr (13.17–21.16 ppm), and Ni (5.53–11.55 ppm) contents. In the Ni versus Cr (Figure 7D), the Cr versus SiO_2 (Figure 7E), and MgO versus SiO_2 (Figure 7F) diagrams, most samples fall within the lower crust partial melting field. In the $\varepsilon_{Nd}(t)$ versus $^{87}Sr/^{86}Sr$ plot (Figure 8), the specimens fall within the adakitic field associated with the thickened magnesian lower crust of southern Tibet.

The Xietongmen adakite samples exhibit enrichment in LILEs and LREEs, showing depletion in HFSEs. These samples exhibit relatively low initial $^{87}Sr/^{86}Sr$ isotopic values (0.7042–0.7044) and positive $\varepsilon_{Nd}(t)$ values (+2.78 to +3.76), with two-stage Nd model ages of 591–670 Ma, indicating that the pluton likely derived from the partial melting of a juvenile lower crust. Additionally, Y/Yb

TABLE 3 Analysis results of whole-rock Sr-Nd isotopic compositions of granite in Xietongmen.

Sample	$^{87}Rb/^{86}Sr$	$^{87}Sr/^{86}Sr$	±2σ	$(^{87}Sr/^{86}Sr)_i$	$^{147}Sm/^{144}Nd$	$^{143}Nd/^{144}Nd$	±2σ	$(^{143}Nd/^{144}Nd)_i$	$\varepsilon_{Nd}(t)$	T_{DM2} (Ma)
XTM-1	1.186900	0.706077	0.000007	0.704458	0.109770	0.512747	0.000007	0.512678	+3.19	637
XTM-2	1.423910	0.706178	0.000006	0.704236	0.097240	0.512768	0.000007	0.512707	+3.76	591
XTM-3	1.421190	0.706255	0.000007	0.704317	0.108740	0.512744	0.000005	0.512676	+3.15	640
XTM-4	1.325010	0.706045	0.000007	0.704238	0.112870	0.512751	0.000005	0.512680	+3.23	633
XTM-6	1.212300	0.706101	0.000006	0.704447	0.197380	0.512781	0.000006	0.512657	+2.78	670

ratios (7.42–10.14; ≈10) and $(Ho/Yb)_N$ ratios (0.73–0.93; ≈1) suggest that amphibole was the principal residual phase in the magma source, with some residual garnet also present (Hu et al., 2014). The high Ba and Sr contents and the slightly positive Eu anomalies suggest that plagioclase did not remain as a residual phase in the source region. The relatively high $Mg^{\#}$ values (> 40) of some samples suggest minor involvement of mantle-derived material during magma evolution. The specimens plot within the crust and mantle field in the (La/Yb) N versus δEu diagram (Figure 9). Therefore, the magma evolution of the Xietongmen adakitic rock was primarily controlled by partial melting, with a residual mineral assemblage dominated by amphibole and garnet, and lacking plagioclase. The geochemical features suggest that the Xietongmen adakite was likely generated through the partial melting of a juvenile thickened lower crust, with a slight input from mantle-sourced components.

6.2 Petrogenesis of the Longger granite

Granites can be categorized into I-, S-, A-, and M-type according to their origin and geological setting (Champion and Chappell, 1992; Chappell and White, 1992). M-type granites formed by fractional crystallization of mantle-derived magma and typically exhibit geochemical characteristics of high $Mg^{\#}$ (50–60) values and low SiO_2 (<65 wt%) contents (Bowden et al., 1979), whereas the Longger granite displays properties of high SiO_2 (66.29–72.58 wt%) contents and low $Mg^{\#}$ (27.88–47.42) values, thus excluding its classification as an M-type granite. The samples exhibit Zr + Nb + Ce + Y concentrations ranging from 180 ppm to 245 ppm and an alkalinity index (AI) of 0.50–0.70, which do not correspond to A-type granites (typically Zr + Nb + Ce + Y ≥ 350 ppm, AI > 0.85) (Whalen et al., 1987; Eby, 1990), thus excluding an A-type granite classification. In the $(Na_2O + K_2O)/CaO$ versus (Zr + Nb + Ce + Y) (Figure 10A) and the $Fe_2O_3^T/Mg$ versus (Zr + Nb + Ce + Y) (Figure 10B) diagrams, the Longger granite plots within the OTG (undifferentiated I, S, M-type granites) granite fields, suggesting that it could be either I-type or S-type granite. The Longger granite is also metaluminous, with an A/CNK ratio of 0.89–1.01. This ratio is below the threshold of 1.1 that distinguishes S-type granite (A/CNK >1.1) and is more consistent with I-type granite (Whalen et al., 1987; Chappell and White, 1992).

Previous research has indicated that P_2O_5, Th, Y, Rb, and other major and trace elements can effectively differentiate I-type and S-type granites (Whalen et al., 1987; Wolf and London, 1994). In S-type granites, P_2O_5 content increases or remains constant with increasing SiO_2 (Whalen et al., 1987; Wolf and London, 1994), whereas in I-type granites, it decreases as SiO_2 increases. Furthermore, I-type granites typically exhibit high concentrations of Th and Y, with Th showing a positive correlation with Rb (Chappell, 1999). The Longger granite samples exhibit a clear negative correlation in the P_2O_5 versus SiO_2 scatter plot, indicating an evolutionary trend characteristic of I-type granites (Figure 10C). Petrographic analysis shows that hornblende, a characteristic mineral of I-type granite, is also present in these samples. The Longger granite is classified as an I-type granite based on these geochemical and mineralogical features.

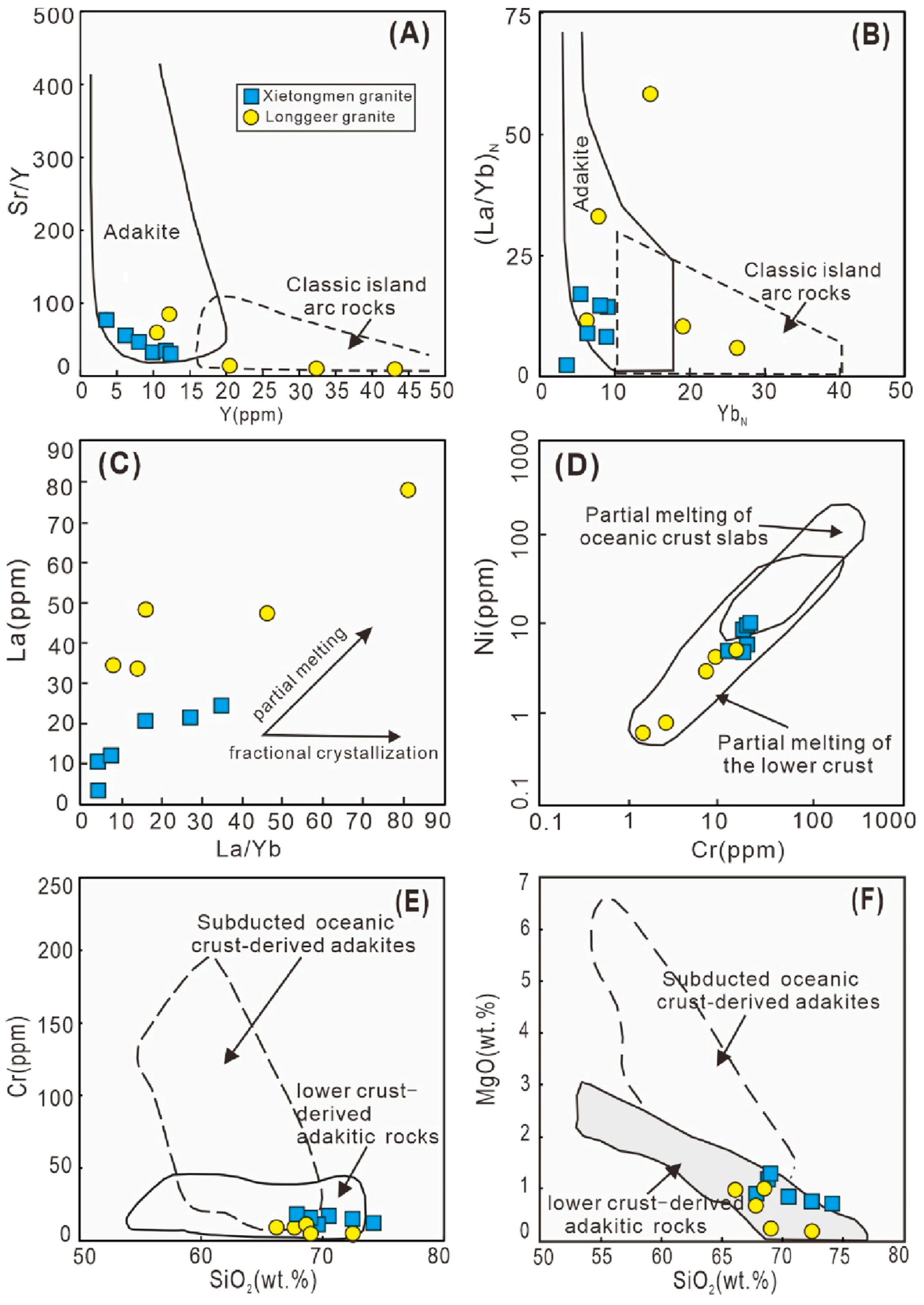

FIGURE 7
(A) Sr/Y vs. Y diagram (Defant and Drummond, 1990); **(B)** $(La/Yb)_N$ vs. Yb_N diagram (Martin, 1999); **(C)** La vs. La/Yb diagram (Furman and Graham, 1999); **(D)** Ni vs. Cr diagram (Wang et al., 2006); **(E)** Cr vs. SiO_2 diagram (Wang et al., 2006); **(F)** MgO vs. SiO_2 diagram (Wang et al., 2006).

10.3389/feart.2025.1597623

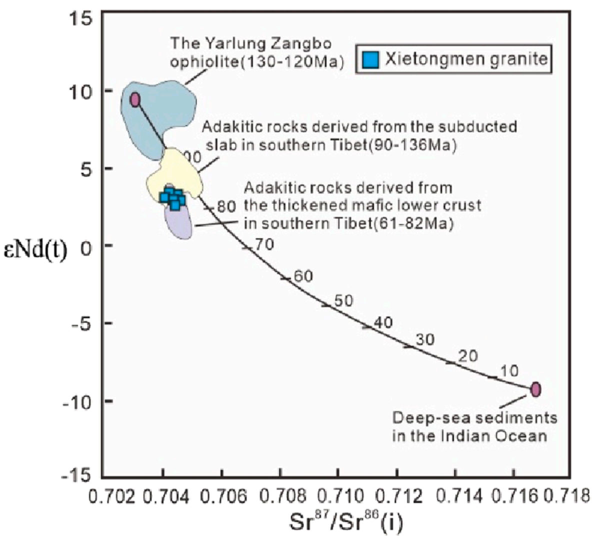

FIGURE 8
ε_{Nd} (t) vs. $^{87}Sr/^{86}Sr$ diagram of the Xietongmen granite (Xu et al., 2020).

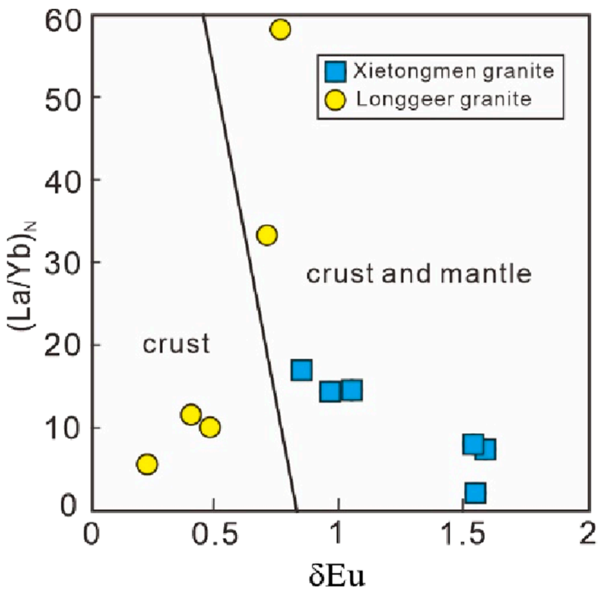

FIGURE 9
$(La/Yb)_N$ vs. δEu diagram (Zhang Z et al., 2014).

I-type granite has been widely regarded as formed through three genetic processes: (1) fractional crystallization of mantle-derived basaltic magma (Cawthorn and Brown, 1976; Wyborn et al., 1987); (2) fractional crystallization of crust-mantle hybrid magma (Turpin et al., 1990; Barbarin, 1996; Chappell et al., 2012); (3) partial melting of the lower crust heated by mantle magma underplating (Castro et al., 1991). I-type granites formed by the first way typically exhibit large-scale coeval basic rocks in their vicinity. However, no extensive basic rocks have been found in the study area. In the La-La/Yb diagram (Figure 7C), the Longger granite exhibits a partial melting trend rather than a fractional crystallization trend. Therefore, the Longger granite was not likely formed by the first one. For the second process, granites formed by crust-mantle mixing typically contain mafic microgranular enclaves, whereas no such dark enclaves have been found in the Longger granite (Turpin et al., 1990; Barbarin, 1996; Chappell et al., 2012). Additionally, the $Mg^{\#}$ values of the Longger granite samples range from 27.88% to 47.42% (mean 38.05%), which do not exhibit the high $Mg^{\#}$ values indicative of interaction with the mantle (Rapp et al., 1999; Hu et al., 2012). Therefore, the Longger granite was not formed in the second way.

The Longger granite samples exhibit high SiO_2 (66.29%–72.58 wt%) and Al_2O_3 (14.64 wt.%–16.27 wt%) contents. They are enriched in K, Rb, Th, U, and Pb, while displaying depletion in Nb, Ta, Ti, and P, indicating a dominantly continental crustal source (Hu et al., 2017). The Th/U ratios (2.3–11.2, mean 8.5) are comparable to those of the lower crust (6.0) (Rudnick and Gao, 2003). As two high-field-strength elements (HFSEs) with similar incompatibility, Nb and Ta remain relatively stable during magmatic evolution, making them effective indicators of magmatic source characteristics and plutonic evolution (Pfänder et al., 2007). All samples of the Longger granite Nb/Ta ratios (5.06–11.06) are lower than those of the depleted mantle (~17) but comparable to those of the continental lower crust (~11) (Pfänder et al., 2007). In the $(La/Yb)_N$ versus δEu diagram (Figure 9), most rock specimens fall within the crustal-type granite region, further supporting a lower crustal origin (Rapp and Watson, 1995; Rudnick and Fountain, 1995). Additionally, the La versus La/Yb (Figure 7C) diagram indicates a distinct partial melting trend, and the Ni versus Cr (Figure 7D), Ni versus SiO_2 (Figure 7E), and MgO versus SiO_2 (Figure 7F) diagrams suggest derivation from lower crustal partial melting. The granite exhibits negative Eu anomalies (δEu = 0.23–0.78) and Ba, Sr depletion characteristics, indicating that it may have undergone plagioclase fractional crystallization (Chappell and White, 1992). In summary, the Longger granite was formed by partial melting of the lower crust. During its magmatic evolution and pluton emplacement, it underwent plagioclase fractional crystallization.

6.3 Tectonic setting and significance

Further insights into the tectonic setting can be derived using granite tectonic classification diagrams (Pearce et al., 1984). In the $Fe_2O_3^{T}/(Fe_2O_3^{T} + MgO)$ versus SiO_2 diagram (Figure 11A), the specimens plot in the island arc granite, continental arc granite, and collisional granite fields. The Rb versus Y + Nb diagram (Figure 11B) places all specimens in the volcanic arc granite field, while the Nb/Zr versus Zr diagram (Figure 11C) indicates a subduction-related setting. Additionally, most samples plot within the active continental margin field in the Th/Yb versus Ta/Yb diagram (Figure 11D). Combining these geochemical characteristics with geochronological data and the contemporaneous tectonic background of Late Cretaceous magmatism, it is evident that both the Xietongmen and Longger granites were emplaced in a subduction-related environment, likely linked to the northward subduction of the Neo-Tethyan oceanic plate beneath the Eurasian continent.

The Late Cretaceous igneous rocks within the Gangdese Tectonic Belt are interpreted as the result of large-scale magmatic activity triggered by the subduction of the Neo-Tethyan oceanic

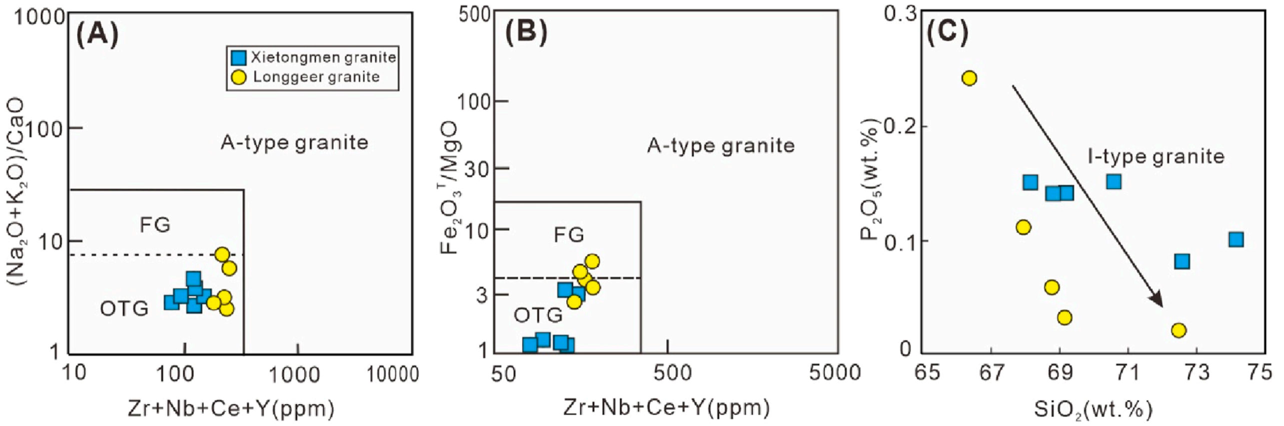

FIGURE 10
(A) $(Na_2O + K_2O)/CaO$ vs. (Zr + Nb + Ce + Y) diagram (Whalen et al., 1987); **(B)** $Fe_2O_3^T/Mg$ vs. (Zr + Nb + Ce + Y) diagram (Whalen et al., 1987); **(C)** P_2O_5 vs. SiO_2 diagram. Abbreviations: FG, highly fractionated I-type granites; OTG, undifferentiated I, S, M-type granites.

plate beneath the Lhasa Block (Murphy, 2019; Tassara et al., 2020; van Hinsbergen et al., 2021; Moyen et al., 2021; Luffi and Ducea, 2022). However, the specific subduction dynamics of the Neo-Tethyan Ocean during this period remain debated, with three prevailing models: (1) flat-slab subduction of the Neo-Tethyan Ocean (Coulon et al., 1986; Wen et al., 2008a; Wen et al., 2008b; Zheng et al., 2014); (2) slab rollback of the Neo-Tethyan oceanic lithosphere (Chung et al., 2005; Ma et al., 2013a; Ma et al., 2013b); (3) ridge subduction of the Neo-Tethyan oceanic lithosphere (Zhang et al., 2010; Zhu et al., 2013).

Wen et al. (2008a), Wen et al. (2008b) collected 25 samples from different regions of the Gangdese tectonic belt, including diorite, granodiorite, gabbro, and granite. Samples emplaced between 103 and 80 Ma were selected for systematic geochemical analysis, and data previously published by Quidellieur et al. (1997) were compiled. The results show that most Late Cretaceous samples exhibit adakitic geochemical characteristics. However, adakitic magmatism likely had a short duration, occurring only over a limited period in a specific tectonic domain. This indicates that the Neo-Tethyan Ocean underwent flat-slab subduction during the Late Cretaceous, followed by slab rollback. In general, flat subduction leads to the expulsion of mantle wedge materials due to compressive forces from the subducting slab, resulting in reduced mantle wedge materials in the subduction zone and thereby inhibiting the formation of mantle-derived mafic magmas. This mechanism is inconsistent with the widespread mafic magmatism reported in the early Late Cretaceous (Gutscher and Peacock, 2003; Kapp et al., 2005; Kapp et al., 2007; Kay et al., 2005; Xu et al., 2015; Zhu et al., 2018).

Ma et al. (2013a), Ma et al. (2014) discovered norites and hypersthene-bearing hornblendites emplaced at ~93 Ma in the Milin area of the southern Gangdese tectonic belt. Geochemical and isotopic data for both rock types indicate that their parental magmas were likely derived from the interaction between upwelling asthenospheric mantle and metasomatized lithospheric mantle (Ma et al., 2013a; Ma et al., 2014). Therefore, they proposed that the early Late Cretaceous magmatic "flare-up" event was triggered by asthenospheric mantle upwelling caused by rollback of the subducted Neo-Tethyan oceanic slab. If the slab rollback mechanism is valid, the oceanic plate should retreat in the direction opposite to subduction. Consequently, magmatic rocks formed during this period should exhibit a progressively younger age trend from north to south. However, such a trend is not observed in the Gangdese Tectonic Belt (Zhu et al., 2009b; Zhu et al., 2018; Zheng et al., 2014).

Zhang et al. (2010) reported high-temperature charnockites formed at 86–90 Ma in the eastern Gangdese Tectonic Belt. Combining coeval calc-alkaline magmatism with the crystallization temperature (900°C) and pressure (1.0 GPa) of the high-temperature *adakitic* charnockites, they proposed that these high-temperature and low-H_2O activity charnockites formed during the subduction of the Neo-Tethyan mid-ocean ridge. Subsequent studies have further supported this model, offering plausible explanations for various geological observations (Zhu et al., 2013; Xu et al., 2015).

Guo et al. (2011), Guo et al. (2013) divided magmatic events in the Gangdese Belt into five stages through zircon U-Pb dating, among which the mid-ocean ridge subduction stage occurred at 89–80 Ma. Based on fieldwork in the Medog-Bomi area, Pan et al. (2014) proposed that the subduction of the mid-ocean ridge beneath the Lhasa Terrane occurred at ~ 95–80 Ma. Zheng et al. (2014) argued that the subduction of the Neo-Tethyan mid-ocean ridge beneath the southern Lhasa Terrane occurred at 105–76 Ma, based on the presence of high-temperature granulite-facies metamorphism and Late Cretaceous basalt basement in the Langxian area, and the resultant heat accumulation caused melting of the overlying crust, leading to a magmatic peak. Ma et al. discovered hypersthene-bearing hornblendites formed at ~93 Ma in the Milin area, whose pressure-temperature (P-T) conditions are consistent with the mid-ocean ridge subduction model. Therefore, for the subduction model of the Neo-Tethyan Ocean during the Late Cretaceous, it can be inferred that a northward mid-ocean ridge subduction regime operated in the early Late Cretaceous.

Most of the above studies also support the southward retreat of the subducting Neo-Tethyan slab beneath the southern Lhasa Terrane during the late Late Cretaceous. However, discrepancies remain regarding the timing of slab rollback, primarily whether it

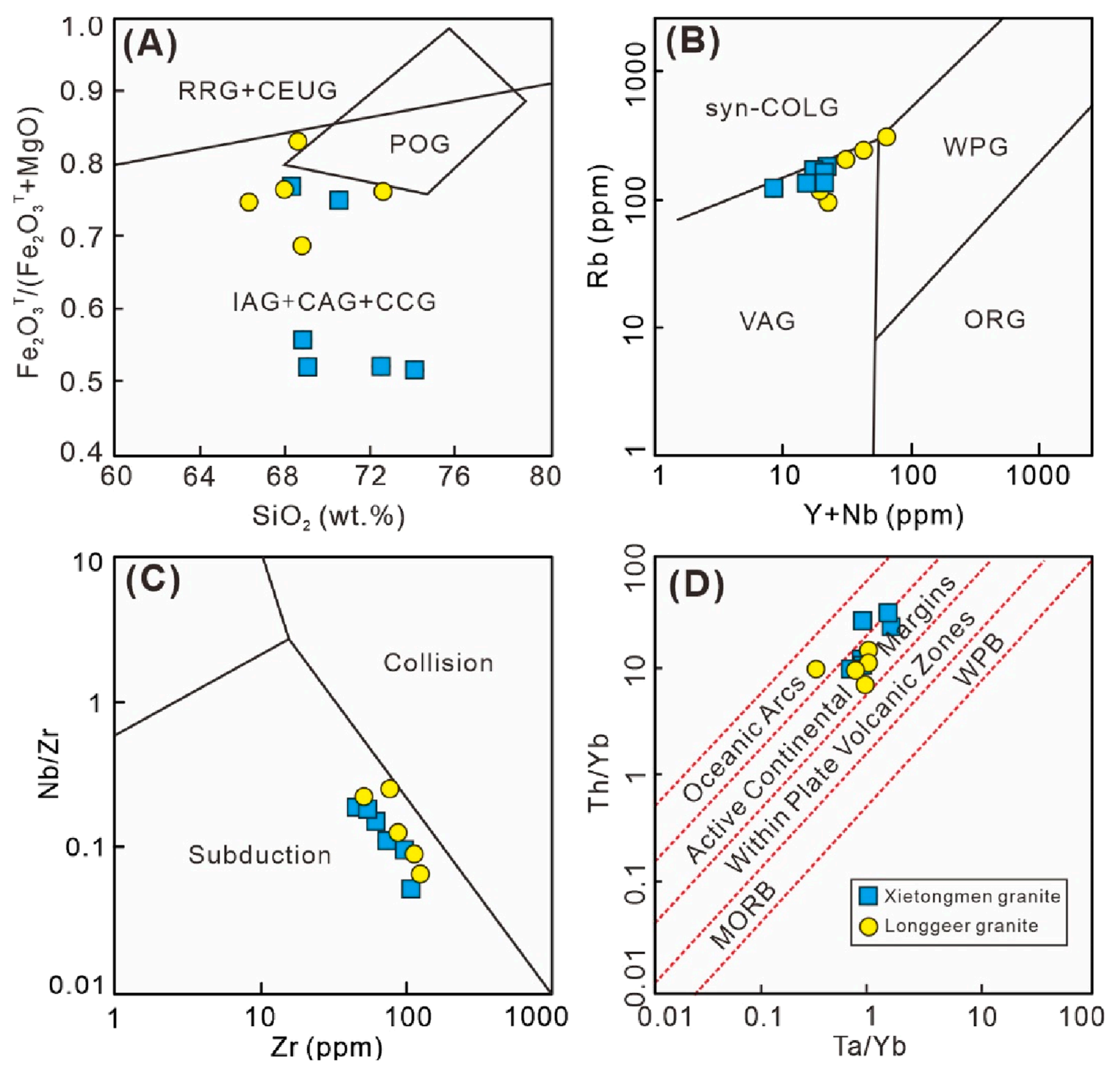

FIGURE 11
(A) $Fe_2O_3^T/(Fe_2O_3^T + MgO)$ vs. SiO_2 diagram (Rollinson H., 1993); **(B)** Rb vs. (Y + Nb) diagram (Pearce et al., 1984); **(C)** Nb/Zr vs. Zr diagram (Pearce et al., 1984); **(D)** Th/Yb vs. Ta/Yb diagram(Schandl and Gorton, 2002). Abbreviations: IAG, Island Arc Granite; CAG, Continental Arc Granite; CCG, Continental Collision Granite; RRG, Rift-Related Granite; CEUG, Continental Epeirogenic Uplift Granite; POG, Post-Collisional Granite; Syn-COLG, Syn-Collisional Granite; VAG, Volcanic Arc Granite; WPG, Within-Plate Granite; ORG, Ocean Ridge Granite.

occurred before ~70 Ma (Chung et al., 2005; Zhang et al., 2010; Ma et al., 2013a; Ma et al., 2013c) or after 70 Ma (Lee et al., 2009; Lee et al., 2012). Therefore, the approximate timing of Neo-Tethyan slab retreat remains unclear (Zhu et al., 2009a; Zhu et al., 2018; Zheng et al., 2014).

These studies show that during the mid-ocean ridge subduction of the Neo-Tethyan Ocean, high-temperature asthenospheric material upwelled through slab windows within the subducted oceanic ridge. These thermal anomalies transferred heat to the lithospheric mantle, raising its temperature. The heated lithospheric mantle then transferred heat to the overlying thickened lower crust, inducing partial melting and ultimately triggering large-scale magmatism. The Xietongmen adakitic rock was likely generated as a product of ridge subduction during this period (Figure 12A). It originated through the partial melting of a thickened lower crust and did not experience significant fractional crystallization. Therefore, its geochemical signatures can serve as an indicator for estimating crustal thickness. According to the crustal thickness estimation formula proposed by Chapman et al. (2015):

$$H = 1.11(Sr/Y) + 8.05 \qquad (1)$$

The Sr/Y values of the selected samples were used to estimate the corresponding crustal thickness, adhering to the applicable range of

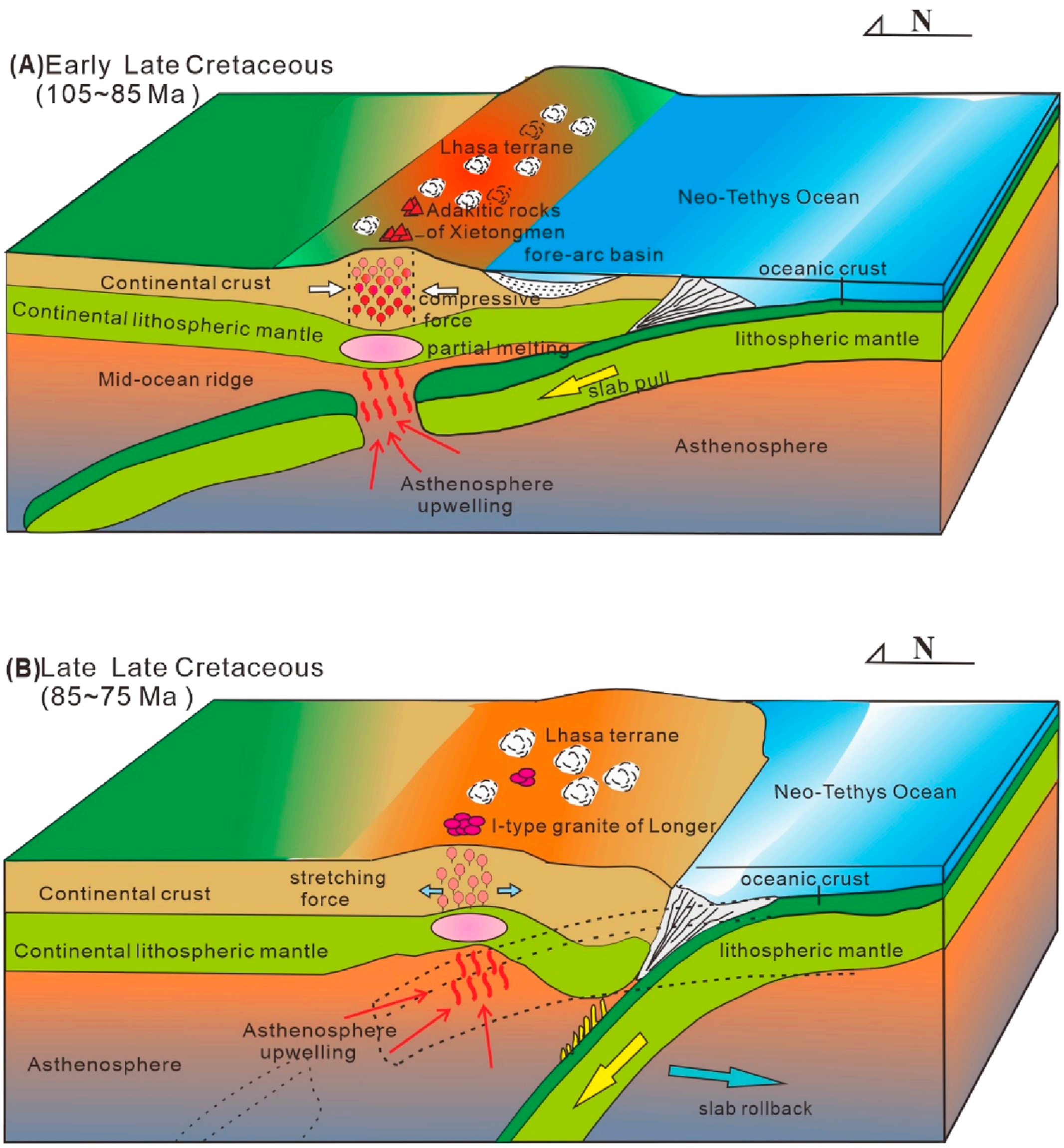

FIGURE 12
Schematic diagrams of **(A)** Subduction of the Neo-Tethyan mid-ocean ridge subduction and **(B)** slab rollback models. (Schematic diagram modified after Suo et al., 2019; Ma et al., 2021).

the formula and the data exclusion criteria. The results show that the median Sr/Y value of the Xietongmen adakitic rock samples is 45.47, yielding an estimated crustal thickness of 49.87 km. Additionally, using the formula proposed by Hu et al. (2017):

$$H = 0.67(Sr/Y) + 28.21 \tag{2}$$

The estimated crustal thickness is 54.10 km. The consistency between these two estimates suggests that the crustal thickness of the Gangdese Tectonic Belt reached approximately 50 km in the early Late Cretaceous. This calculation result aligns with the conclusion of Zhu et al. (2023) based on a comprehensive analysis of petrological, geochemical, and geochronological data, which states that "the Gangdese crust experienced local thickening at ~90 Ma."

Calculating with Equations 1, 2, the estimated crustal thickness for forming the Longger I-type granite is 33.74 km and 43.86 km. Both values are lower than those for the Xietongmen adakitic rock, suggesting that the Longger I-type granite formed in a relatively extensional setting with a thinner crust, in contrast to the thickened crustal environment of the Xietongmen adakitic rock.

Thus, the Xietongmen adakitic rock, developed in the early Late Cretaceous of the Gangdese Belt, formed under a crustal thickening regime, while the Longger I-type granite, emplaced in the late Late Cretaceous, formed under conditions of crustal thinning. Ridge subduction likely occurred in the initial phase of the Late Cretaceous, followed by slab rollback in the late Late Cretaceous. The slab rollback facilitated extensive asthenospheric mantle upwelling and underplating, which thermally perturbed the lithospheric mantle. The heated lithospheric mantle subsequently transferred heat to the lower crust, causing partial melting and the formation of Longger I-type granite, which is primarily crustal-derived (Figure 12B). This interpretation is consistent with previous studies on crustal recycling in the Gangdese Belt (Chung et al., 2005; Zhang et al., 2010; Ma et al., 2013a; 2013b). However, this hypothesis requires further testing.

7 Conclusion

(1) Zircon U-Pb age analysis indicates that the Xietongmen granite and Longger granite in the Gangdese Tectonic belt have ages of 95.9 ± 0.6 Ma and 79.5 ± 0.4 Ma, respectively, suggesting that both intrusions were emplaced during the Late Cretaceous.
(2) The Xietongmen granite belongs to the high-K calc-alkaline, metaluminous granite series. Furthermore, the samples are enriched in Sr and depleted in Y, with high Sr/Y and $(La/Yb)_N$ ratios, exhibiting geochemical characteristics typical of adakitic rocks. Petrogenetically, this granite originated from the partial melting of the thickened lower crust.
(3) The Longger granite is a metaluminous granitoid of the high-K calc-alkaline series. Geochemically, the pluton exhibits enrichment in large ion lithophile elements (LILE) and depletion in high field strength elements (HFSE), and displays geochemical features of I-type granites. Petrogenetically, it originated from the partial melting of the lower crust.
(4) The Xietongmen granite was likely formed in the early Late Cretaceous in a tectonic environment linked to the subduction of the Neo-Tethyan oceanic ridge. In contrast, the Longger I-type granite was likely emplaced in the late Late Cretaceous, following ridge subduction and during the slab rollback phase.

Data availability statement

The original contributions presented in the study are included in the article/supplementary material, further inquiries can be directed to the corresponding author.

Author contributions

FZ: Conceptualization, Writing – review and editing, Methodology, Writing – original draft. XZ: Software, Data curation, Writing – review and editing, Writing – original draft, Investigation. ZG: Writing – original draft, Software, Data curation. EW: Data curation, Writing – original draft, Investigation. HW: Software, Writing – original draft, Investigation.

Funding

The author(s) declare that financial support was received for the research and/or publication of this article. This work was supported by the Second Qinghai-Tibet Plateau Scientific Expedition and Research Project (No. 2019QZKK0901).

Conflict of interest

The authors declare that the research was conducted in the absence of any commercial or financial relationships that could be construed as a potential conflict of interest.

Generative AI statement

The author(s) declare that no Generative AI was used in the creation of this manuscript.

Publisher's note

References

Atherton, M. P., and Petford, N. (1993). Generation of sodium-rich magmas from newly underplated basaltic crust. *Nature* 362 (6416), 144–146. doi:10.1038/362144a0

Baral, U., Lin, D., Goswami, T. K., Sarma, M., Qasim, M., and Bezbaruah, D. (2019). Detrital zircon U–Pb geochronology of a Cenozoic foreland basin in Northeast India: implications for zircon provenance during the collision of the Indian and Asian plates. *Terra nova.* 31 (1), 18–27. doi:10.1111/ter.12364

Barbarin, B. (1996). Genesis of the two main types of peraluminous granitoids. *Geology* 24 (4), 295–298. doi:10.1130/0091-7613(1996)024<0295:GOTTMT>2.3.CO;2

Bowden, P., Bennett, J. N., Whitley, J. E., and Moyes, A. B. (1979). Rare earths in Nigerian mesozoic granites and related rocks. *Phys. Chem. Earth* 11, 479–491. doi:10.1016/0079-1946(79)90045-4

Castillo, P. R. (2006). An overview of adakite petrogenesis. *Chin. Sci. Bull.* 51 (3), 257–268. doi:10.1007/s11434-006-0257-7

Castro, A., Moreno-Ventas, I., and de la Rosa, J. D. (1991). H-type (hybrid) granitoids: a proposed revision of the granite-type classification and nomenclature. *Earth-Science Rev.* 31 (3), 237–253. doi:10.1016/0012-8252(91)90020-G

Cawthorn, R. G., and Brown, P. A. (1976). A model for the formation and crystallization of corundum-normative calc-alkaline magmas through amphibole fractionation. *J. Geol.* 84 (4), 467–476. doi:10.1086/628212

Champion, D. C., and Chappell, B. W. (1992). Petrogenesis of felsic I-type granites: an example from northern Queensland. *Earth Environ. Sci. Trans. R. Soc. Edinb.* 83 (1-2), 115–126. doi:10.1017/S026359330000780X

Chapman, J. B., Ducea, M. N., DeCelles, P. G., and Profeta, L. (2015). Tracking changes in crustal thickness during orogenic evolution with Sr/Y: an example from the North American Cordillera. *Geology* 43 (10), 919–922. doi:10.1130/G36996.1

Chappell, B. W. (1999). Aluminium saturation in I- and S-type granites and the characterization of fractionated haplogranites. *Lithos* 46 (3), 535–551. doi:10.1016/S0024-4937(98)00086-3

Chappell, B. W., Bryant, C. J., and Wyborn, D. (2012). Peraluminous I-type granites. *Lithos* 153, 142–153. doi:10.1016/j.lithos.2012.07.008

Chappell, B. W., and White, A. J. R. (1992). I- and S-type granites in the lachlan fold belt. *Earth Environ. Sci. Trans. R. Soc. Edinb.* 83 (1-2), 1–26. doi:10.1017/S0263593300007720

Chu, M., Chung, S., Song, B., Liu, D., O'Reilly, S. Y., Pearson, N. J., et al. (2006). Zircon U-Pb and Hf isotope constraints on the Mesozoic tectonics and crustal evolution of southern Tibet. *Geology* 34 (9), 745–748. doi:10.1130/G22725.1

Chung, S., Chu, M., Zhang, Y., Xie, Y., Lo, C., Lee, T., et al. (2005). Tibetan tectonic evolution inferred from spatial and temporal variations in post-collisional magmatism. *Earth-Science Rev.* 68 (3), 173–196. doi:10.1016/j.earscirev.2004.05.001

Chung, S., Liu, D., Ji, J., Chu, M., Lee, H., Wen, D., et al. (2003). Adakites from continental collision zones: melting of thickened lower crust beneath southern Tibet. *Geology* 31 (11), 1021–1024. doi:10.1130/G19796.1

Collins, W. J., Murphy, J. B., Johnson, T. E., and Huang, H. (2020). Critical role of water in the formation of continental crust. *Nat. Geosci.* 13 (5), 331–338. doi:10.1038/s41561-020-0573-6

Coulon, C., Maluski, H., Bollinger, C., and Wang, S. (1986). Mesozoic and cenozoic volcanic rocks from central and southern Tibet:39Ar-40Ar dating, petrological characteristics and geodynamical significance. *Earth Planet. Sci. Lett.* 79 (3), 281–302. doi:10.1016/0012-821X(86)90186-X

Defant, M. J., and Drummond, M. S. (1990). Derivation of some modern arc magmas by melting of young subducted lithosphere. *Nature* 347 (6294), 662–665. doi:10.1038/347662a0

DePaolo, D. J., Harrison, T. M., Wielicki, M., Zhao, Z., Zhu, D., Zhang, H., et al. (2019). Geochemical evidence for thin syn-collision crust and major crustal thickening between 45 and 32 Ma at the southern margin of Tibet. *Gondwana Res.* 73, 123–135. doi:10.1016/j.gr.2019.03.011

Ding, L., Xu, Q., Yue, Y., Wang, H., Cai, F., and Li, S. (2014). The andean-type gangdese mountains: paleoelevation record from the paleocene–eocene linzhou basin. *Earth Planet. Sci. Lett.* 392, 250–264. doi:10.1016/j.epsl.2014.01.045

Ducea, M. N., Chapman, A. D., Bowman, E., and Triantafyllou, A. (2021). Arclogites and their role in continental evolution; part 1: background, locations, petrography, geochemistry, chronology and thermobarometry. *Earth-Science Rev.* 214, 103375. doi:10.1016/j.earscirev.2020.103375

Eby, G. N. (1990). The A-type granitoids: a review of their occurrence and chemical characteristics and speculations on their petrogenesis. *Lithos* 26 (1), 115–134. doi:10.1016/0024-4937(90)90043-Z

Furman, T., and Graham, D. (1999). Erosion of lithospheric mantle beneath the East African Rift system: geochemical evidence from the Kivu volcanic province. *Lithos* 48 (1), 237–262. doi:10.1016/S0024-4937(99)00031-6

Gibbons, A. D., Zahirovic, S., Müller, R. D., Whittaker, J. M., and Yatheesh, V. (2015). A tectonic model reconciling evidence for the collisions between India, Eurasia and intra-oceanic arcs of the central-eastern Tethys. *Gondwana Res.* 28 (2), 451–492. doi:10.1016/j.gr.2015.01.001

Guo, L., Zhang, H., Harris, N., Pan, F., and Xu, W. (2011). Origin and evolution of multi-stage felsic melts in eastern Gangdese belt: constraints from U–Pb zircon dating and Hf isotopic composition. *Lithos* 127 (1), 54–67. doi:10.1016/j.lithos.2011.08.005

Guo, L., Zhang, H., Harris, N., Pan, F., and Xu, W. (2013). Late Cretaceous (~81Ma) high-temperature metamorphism in the southeastern Lhasa terrane: implication for the Neo-Tethys ocean ridge subduction. *Tectonophysics* 608, 112–126. doi:10.1016/j.tecto.2013.10.007

Gutscher, M., and Peacock, S. M. (2003). Thermal models of flat subduction and the rupture zone of great subduction earthquakes. *J. Geophys. Res. Solid Earth* 108 (B1), 1–2. doi:10.1029/2001JB000787

Hoskin, P. W. O., and Ireland, T. R. (2000). Rare earth element chemistry of zircon and its use as a provenance indicator. *Geology* 28 (7), 627–630. doi:10.1130/0091-7613(2000)28<627:REECOZ>2.0.CO;2

Hou, Z., Duan, L., Lu, Y., Zheng, Y., Zhu, D., Yang, Z., et al. (2015). Lithospheric architecture of the Lhasa terrane and its control on ore deposits in the himalayan-Tibetan orogen. *Econ. Geol. Geol.* 110 (6), 1541–1575. doi:10.2113/econgeo.110.6.1541

Hou, Z., Zheng, Y., Yang, Z., Rui, Z., Zhao, Z., Jiang, S., et al. (2013). Contribution of mantle components within juvenile lower-crust to collisional zone porphyry Cu systems in Tibet. *Miner. Deposita* 48 (2), 173–192. doi:10.1007/s00126-012-0415-6

Hu, F., Ducea, M. N., Liu, S., and Chapman, J. B. (2017). Quantifying crustal thickness in continental collisional belts: global perspective and a geologic application. *Sci. Rep.* 7 (1), 7058. doi:10.1038/s41598-017-07849-7

Hu, J., Jiang, S., Zhao, H., Shao, Y., Zhang, Z., Xiao, E., et al. (2012). Geochemistry and petrogenesis of the Huashan granites and their implications for the Mesozoic tectonic settings in the Xiaoqinling gold mineralization belt, NW China. *J. Asian Earth Sci.* 56, 276–289. doi:10.1016/j.jseaes.2012.05.016

Hu, Z., Yang, X., Duan, L., and Sun, W. (2014). Geochronological and geochemical constraints on genesis of the adakitic rocks in outang, south tan–Lu fault belt (northeastern yangtze block). *Tectonophysics* 626, 86–104. doi:10.1016/j.tecto.2014.04.004

Ingalls, M., Rowley, D. B., Currie, B., and Colman, A. S. (2016). Large-scale subduction of continental crust implied by India–Asia mass-balance calculation. *Nat. Geosci.* 9 (11), 848–853. doi:10.1038/ngeo2806

Ji, W., Wu, F., Chung, S., Li, J., and Liu, C. (2009). Zircon U–Pb geochronology and Hf isotopic constraints on petrogenesis of the Gangdese batholith, southern Tibet. *Chem. Geol.* 262 (3), 229–245. doi:10.1016/j.chemgeo.2009.01.020

Ji, W., Wu, F., Chung, S., and Liu, C. (2014). The Gangdese magmatic constraints on a latest Cretaceous lithospheric delamination of the Lhasa terrane, southern Tibet. *Lithos* 210-211, 168–180. doi:10.1016/j.lithos.2014.10.001

Kang, Z., Xu, J., Wilde, S. A., Feng, Z., Chen, J., Wang, B., et al. (2014). Geochronology and geochemistry of the Sangri group volcanic rocks, southern Lhasa terrane: implications for the early subduction history of the neo-tethys and gangdese magmatic arc. *Lithos* 200-201, 157–168. doi:10.1016/j.lithos.2014.04.019

Kapp, P., DeCelles, P. G., Gehrels, G. E., Heizler, M., and Ding, L. (2007). Geological records of the lhasa-qiangtang and indo-asian collisions in the nima area of central Tibet. *GSA Bull.* 119 (7-8), 917–933. doi:10.1130/B26033.1

Kapp, P., Yin, A., Harrison, T. M., and Ding, L. (2005). Cretaceous-Tertiary shortening, basin development, and volcanism in central Tibet. *GSA Bull. Bull.* 117 (7-8), 865–878. doi:10.1130/B25595.1

Kay, S. M., Godoy, E., and Kurtz, A. (2005). Episodic arc migration, crustal thickening, subduction erosion, and magmatism in the south-central Andes. *GSA Bull.* 117 (1-2), 67–88. doi:10.1130/B25431.1

Lai, S., and Qin, J. (2013). Adakitic rocks derived from the partial melting of subducted continental crust: evidence from the Eocene volcanic rocks in the northern Qiangtang block. *Gondwana Res.* 23 (2), 812–824. doi:10.1016/j.gr.2012.06.003

Lee, H., Chung, S., Ji, J., Qian, Q., Gallet, S., Lo, C., et al. (2012). Geochemical and Sr–Nd isotopic constraints on the genesis of the Cenozoic Linzizong volcanic successions, southern Tibet. *J. Asian Earth Sci.* 53, 96–114. doi:10.1016/j.jseaes.2011.08.019

Lee, H., Chung, S., Lo, C., Ji, J., Lee, T., Qian, Q., et al. (2009). Eocene Neotethyan slab breakoff in southern Tibet inferred from the Linzizong volcanic record. *Tectonophysics* 477 (1), 20–35. doi:10.1016/j.tecto.2009.02.031

Luffi, P., and Ducea, M. N. (2022). Chemical mohometry: assessing crustal thickness of ancient orogens using geochemical and isotopic data. *Rev. Geophys.* 60 (2), e2021RG000753. doi:10.1029/2021RG000753

Ma, L., Wang, B., Jiang, Z., Wang, Q., Li, Z., Wyman, D. A., et al. (2014). Petrogenesis of the Early Eocene adakitic rocks in the Napuri area, southern Lhasa: partial melting of thickened lower crust during slab break-off and implications for crustal thickening in southern Tibet. *Lithos* 196-197, 321–338. doi:10.1016/j.lithos.2014.02.011

Ma, L., Wang, Q., Li, Z., Wyman, D. A., Jiang, Z., Yang, J., et al. (2013a). Early Late Cretaceous (ca. 93Ma) norites and hornblendites in the Milin area, eastern Gangdese: lithosphere–asthenosphere interaction during slab roll-back and an insight into early Late Cretaceous (ca. 100–80Ma) magmatic "flare-up" in southern Lhasa (Tibet). *Lithos* 172-173, 17–30. doi:10.1016/j.lithos.2013.03.007

Ma, L., Wang, Q., Wyman, D. A., Jiang, Z., Yang, J., Li, Q., et al. (2013b). Late Cretaceous crustal growth in the Gangdese area, southern Tibet: petrological and Sr–Nd–Hf–O isotopic evidence from Zhengga diorite–gabbro. *Chem. Geol.* 349-350, 54–70. doi:10.1016/j.chemgeo.2013.04.005

Ma, L., Wang, Q., Wyman, D. A., Li, Z., Jiang, Z., Yang, J., et al. (2013c). Late Cretaceous (100–89Ma) magnesian charnockites with adakitic affinities in the Milin area, eastern Gangdese: partial melting of subducted oceanic crust and implications for crustal growth in southern Tibet. *Lithos* 175-176, 315–332. doi:10.1016/j.lithos.2013.04.006

Ma, X., Xu, Z., Liu, F., Zhoa, Z., and Li, H. (2021). Episodic magmatism in continental arcs and crustal thickening: a case study of the gangdese arc in southern Tibet. *Acta Geol. Sin.* 95 (1), 107–123. doi:10.3969/j.issn.0001-5717

Ma, X., Xu, Z., Zhao, Z., and Yi, Z. (2019). Identification of a new source for the Triassic Langjiexue Group: evidence from a gabbro-diorite complex in the Gangdese magmatic belt and zircon microstructures from sandstones in the Tethyan Himalaya, southern Tibet. *Geosphere* 16 (1), 407–434. doi:10.1130/GES02154.1

Macpherson, C. G., Dreher, S. T., and Thirlwall, M. F. (2006). Adakites without slab melting: high pressure differentiation of island arc magma, Mindanao, the Philippines. *Earth Planet. Sci. Lett.* 243 (3), 581–593. doi:10.1016/j.epsl.2005.12.034

Maniar, P. D., and Piccoli, P. M. (1989). Tectonic discrimination of granitoids. *GSA Bull.* 101 (5), 635–643. doi:10.1130/0016-7606(1989)101<0635:TDOG>2.3.CO;2

Martin, H. (1999). Adakitic magmas: modern analogues of Archaean granitoids. *Lithos* 46 (3), 411–429. doi:10.1016/S0024-4937(98)00076-0

Middlemost, E. A. K. (1994). Naming materials in the magma/igneous rock system. *Earth-Science Rev.* 37 (3), 215–224. doi:10.1016/0012-8252(94)90029-9

Moyen, J., Janoušek, V., Laurent, O., Bachmann, O., Jacob, J., Farina, F., et al. (2021). Crustal melting vs. fractionation of basaltic magmas: Part 1, granites and paradigms. *Lithos* 402-403, 106291. doi:10.1016/j.lithos.2021.106291

Murphy, J. B. (2019). Appinite suites and their genetic relationship with coeval voluminous granitoid batholiths. *Int. Geol. Rev.* 62, 683–713. doi:10.1080/00206814.2019.1630859

Pan, F., Zhang, H., Xu, W., Guo, L., Wang, S., and Luo, B. (2014). U–Pb zircon chronology, geochemical and Sr–Nd isotopic composition of Mesozoic–Cenozoic granitoids in the SE Lhasa terrane: petrogenesis and tectonic implications. *Lithos* 192-195, 142–157. doi:10.1016/j.lithos.2014.02.005

Pearce, J. A., Harris, N. B. W., and Tindle, A. G. (1984). Trace element discrimination diagrams for the tectonic interpretation of granitic rocks. *J. Petrology* 25 (4), 956–983. doi:10.1093/petrology/25.4.956

Pfänder, J. A., Münker, C., Stracke, A., and Mezger, K. (2007). Nb/Ta and Zr/Hf in ocean island basalts — implications for crust–mantle differentiation and the fate of Niobium. *Earth Planet. Sci. Lett.* 254 (1), 158–172. doi:10.1016/j.epsl.2006.11.027

Qasim, M., Ding, L., Khan, M. A., Jadoon, I. A. K., Haneef, M., Baral, U., et al. (2018). Tectonic implications of detrital zircon ages from lesser himalayan mesozoic-cenozoic strata, Pakistan. *Geochem. Geophys. Geosystems* 19 (5), 1636–1659. doi:10.1002/2017GC006895

Quidelleur, X., Grove, M., Lovera, O. M., Harrison, T. M., Yin, A., and Ryerson, F. J. (1997). Thermal evolution and slip history of the renbu zedong thrust, southeastern Tibet. *J. Geophys. Res. Solid Earth* 102 (B2), 2659–2679. doi:10.1029/96JB02483

Ran, M., Kang, Z., Xu, J., Yang, F., Jiang, Z., Li, Q., et al. (2019). Evolution of the northward subduction of the neo-tethys: implications of geochemistry of cretaceous arc volcanics in Qinghai-Tibetan plateau. *Palaeogeogr. Palaeoclimatol. Palaeoecol.* 515, 83–94. doi:10.1016/j.palaeo.2017.12.043

Rapp, R. P., Shimizu, N., Norman, M. D., and Applegate, G. S. (1999). Reaction between slab-derived melts and peridotite in the mantle wedge: experimental constraints at 3.8 GPa. *Chem. Geol.* 160 (4), 335–356. doi:10.1016/S0009-2541(99)00106-0

Rapp, R. P., and Watson, E. B. (1995). Dehydration melting of metabasalt at 8–32 kbar: implications for continental growth and crust-mantle recycling. *J. Petrology* 36 (4), 891–931. doi:10.1093/petrology/36.4.891

Rickwood, P. C. (1989). Boundary lines within petrologic diagrams which use oxides of major and minor elements. *Lithos* 22 (4), 247–263. doi:10.1016/0024-4937(89)90028-5

Rollinson, H. (1993). *Using geochemical data: evaluation, presentation, interpretation*. Wiley. doi:10.4324/9781315845548

Rowley, D. B. (2019). Comparing paleomagnetic study means with apparent wander paths: a case study and paleomagnetic test of the greater India versus greater Indian basin hypotheses. *Tectonics* 38 (2), 722–740. doi:10.1029/2017TC004802

Rudnick, R. L., and Fountain, D. M. (1995). Nature and composition of the continental crust: a lower crustal perspective. *Rev. Geophys.* 33 (3), 267–309. doi:10.1029/95RG01302

Rudnick, R. L., and Gao, S. (2003). "Composition of the continental crust," in *Treatise on geochemistry*. Editors H. D. Holland, and K. K. Turekian (Oxford: Pergamon), 1–64. doi:10.1016/B0-08-043751-6/03016-4

Schandl, E. S., and Gorton, M. P. (2002). Application of high field strength elements to discriminate tectonic settings in vms environments. *Econ. Geol.* 97 (3), 629–642. doi:10.2113/gsecongeo.97.3.629

Schärer, U., Xu, R., and Allègre, C. J. (1984). UPb geochronology of gangdese (transhimalaya) plutonism in the lhasa-xigaze region, Tibet. *Earth Planet. Sci. Lett.* 69 (2), 311–320. doi:10.1016/0012-821X(84)90190-0

Sun, S. S., and McDonough, W. F. (1989). *Chemical and isotopic systematics of oceanic basalts: implications for mantle composition and processes.* London: Geological Society of London 7. 42, 313–345. doi:10.1144/GSL.SP.1989.042.01.19

Suo, Y., Li, S., Jin, C., Zhang, Y., Zhou, J., Li, X., et al. (2019). Eastward tectonic migration and transition of the Jurassic-Cretaceous Andean-type continental margin along Southeast China. *Earth-Science Rev.* 196, 102884. doi:10.1016/j.earscirev.2019.102884

Tang, S., Dong, S., Yang, X., Fan, C., Li, H., Zhong, Z., et al. (2023). Geochemical analysis of dolomite in the fourth member of the upper sinian dengying formation, northern sichuan basin, China. *ACS Omega* 8 (48), 45878–45895. doi:10.1021/acsomega.3c06638

Tassara, S., Ague, J. J., and Valencia, V. (2020). The deep magmatic cumulate roots of the Acadian orogen, eastern North America. *Geology* 49 (2), 168–173. doi:10.1130/G47887.1

Taylor, S. R., and McLennan, S. M. (1995). The geochemical evolution of the continental crust. *Rev. Geophys.* 33 (2), 241–265. doi:10.1029/95RG00262

Turpin, L., Cuney, M., Friedrich, M., Bouchez, J., and Aubertin, M. (1990). Meta-igneous origin of Hercynian peraluminous granites in N.W. French Massif Central: implications for crustal history reconstructions. *Contributions Mineralogy Petrology* 104 (2), 163–172. doi:10.1007/BF00306440

van Hinsbergen, D. J. J., Lippert, P. C., Li, S., Huang, W., Advokaat, E. L., and Spakman, W. (2019). Reconstructing Greater India: paleogeographic, kinematic, and geodynamic perspectives. *Tectonophysics* 760, 69–94. doi:10.1016/j.tecto.2018.04.006

van Hinsbergen, D. J. J., Steinberger, B., Guilmette, C., Maffione, M., Gürer, D., Peters, K., et al. (2021). A record of plume-induced plate rotation triggering subduction initiation. *Nat. Geosci.* 14, 626–630. doi:10.1038/s41561-021-00780-7

Wang, C., Ding, L., Zhang, L., Kapp, P., Pullen, A., and Yue, Y. (2016). Petrogenesis of Middle–Late Triassic volcanic rocks from the Gangdese belt, southern Lhasa terrane: implications for early subduction of Neo-Tethyan oceanic lithosphere. *Lithos* 262, 320–333. doi:10.1016/j.lithos.2016.07.021

Wang, Q., Wyman, D. A., Xu, J., Dong, Y., Vasconcelos, P. M., Pearson, N., et al. (2008). Eocene melting of subducting continental crust and early uplifting of central Tibet: evidence from central-western Qiangtang high-K calc-alkaline andesites, dacites and rhyolites. *Earth Planet. Sci. Lett.* 272 (1), 158–171. doi:10.1016/j.epsl.2008.04.034

Wang, Q., Xu, J., Jian, P., Bao, Z., Zhao, Z., Li, C., et al. (2006). Petrogenesis of adakitic porphyries in an extensional tectonic setting, dexing, south China: implications for the genesis of porphyry copper mineralization. *J. Petrology* 47 (1), 119–144. doi:10.1093/petrology/egi070

Wang, Q., Zhu, D., Zhao, Z., Liu, S., Chung, S., Li, S., et al. (2014). Origin of the ca. 90Ma magnesia-rich volcanic rocks in SE Nyima, central Tibet: products of lithospheric delamination beneath the Lhasa-Qiangtang collision zone. *Lithos* 198-199, 24–37. doi:10.1016/j.lithos.2014.03.019

Webb, A. A. G., Guo, H., Clift, P. D., Husson, L., Müller, T., Costantino, D., et al. (2017). The Himalaya in 3D: slab dynamics controlled mountain building and monsoon intensification. *Lithosphere* 9 (4), L636.1–651. doi:10.1130/L636.1

Wen, D., Chung, S., Song, B., Iizuka, Y., Yang, H., Ji, J., et al. (2008). Late Cretaceous Gangdese intrusions of adakitic geochemical characteristics, SE Tibet: petrogenesis and tectonic implications. *Lithos* 105 (1), 1–11. doi:10.1016/j.lithos.2008.02.005

Wen, D., Liu, D., Chung, S., Chu, M., Ji, J., Zhang, Q., et al. (2008). Zircon SHRIMP U–Pb ages of the gangdese batholith and implications for neotethyan subduction in southern Tibet. *Chem. Geol.* 252 (3), 191–201. doi:10.1016/j.chemgeo.2008.03.003

Whalen, J. B., Currie, K. L., and Chappell, B. W. (1987). A-type granites: geochemical characteristics, discrimination and petrogenesis. *Contributions Mineralogy Petrology* 95 (4), 407–419. doi:10.1007/BF00402202

Wolf, M. B., and London, D. (1994). Apatite dissolution into peraluminous haplogranitic melts: an experimental study of solubilities and mechanisms. *Geochimica Cosmochimica Acta* 58 (19), 4127–4145. doi:10.1016/0016-7037(94)90269-0

Wyborn, D., Turner, B. S., and And Chappell, B. W. (1987). The Boggy Plain Supersuite: a distinctive belt of I-type igneous rocks of potential economic significance in the Lachlan Fold Belt. *Aust. J. Earth Sci.* 34 (1), 21–43. doi:10.1080/08120098708729392

Xu, Q., Zeng, L., Zhao, L., Hu, Z., Wang, H., Shen, Y., et al. (2020). Geochemical characteristics and petrogenesis of Miocene high Sr/Y rocks in Xigatze fore-arc basin, southern Tibet. *Lithos* 366-367, 105543. doi:10.1016/j.lithos.2020.105543

Xu, W., Zhang, H., Luo, B., Guo, L., and Yang, H. (2015). Adakite-like geochemical signature produced by amphibole-dominated fractionation of arc magmas: an example from the Late Cretaceous magmatism in Gangdese belt, south Tibet. *Lithos* 232, 197–210. doi:10.1016/j.lithos.2015.07.001

Xu, Z., Dilek, Y., Cao, H., Yang, J., Robinson, P., Ma, C., et al. (2015). Paleo-tethyan evolution of Tibet as recorded in the east cimmerides and west cathaysides. *J. Asian Earth Sci.* 105, 320–337. doi:10.1016/j.jseaes.2015.01.021

Yin, A., and Harrison, T. M. (2000). Geologic evolution of the himalayan-Tibetan orogen. *Annu. Rev. Earth Planet. Sci.* 28 (28), 211–280. doi:10.1146/annurev.earth.28.1.211

Zhang, K., Zhang, Y., Tang, X., and Xia, B. (2012). Late Mesozoic tectonic evolution and growth of the Tibetan plateau prior to the Indo-Asian collision. *Earth-Science Rev.* 114 (3), 236–249. doi:10.1016/j.earscirev.2012.06.001

Zhang, S., Li, F., Li, Y., Liu, W., and Qin, Y. (2014). Early Ordovician strongly peraluminous granite in the middle section of the Yarlung Zangbo junction zone and its geological significance. *Sci. China Earth Sci.* 57 (4), 630–643. doi:10.1007/s11430-013-4721-3

Zhang, Z., Dong, X., Xiang, H., He, Z., and Liou, J. G. (2014). Metagabbros of the Gangdese arc root, south Tibet: implications for the growth of continental crust. *Geochimica Cosmochimica Acta* 143, 268–284. doi:10.1016/j.gca.2014.01.045

Zhang, Z., Zhao, G., Santosh, M., Wang, J., Dong, X., and Shen, K. (2010). Late Cretaceous charnockite with adakitic affinities from the Gangdese batholith, southeastern Tibet: evidence for Neo-Tethyan mid-ocean ridge subduction? *Gondwana Res.* 17 (4), 615–631. doi:10.1016/j.gr.2009.10.007

Zheng, Y., Hou, Z., Gong, Y., Liang, W., Sun, Q., Zhang, S., et al. (2014). Petrogenesis of Cretaceous adakite-like intrusions of the Gangdese Plutonic Belt, southern Tibet: implications for mid-ocean ridge subduction and crustal growth. *Lithos* 190-191, 240–263. doi:10.1016/j.lithos.2013.12.013

Zhu, D., Mo, X., Niu, Y., Zhao, Z., Wang, L., Liu, Y., et al. (2009). Geochemical investigation of Early Cretaceous igneous rocks along an east–west traverse throughout the central Lhasa Terrane, Tibet. *Chem. Geol.* 268 (3), 298–312. doi:10.1016/j.chemgeo.2009.09.008

Zhu, D., Pan, G., Chung, S., Liao, Z., Wang, L., and And Li, G. (2008). SHRIMP zircon age and geochemical constraints on the origin of lower jurassic volcanic rocks from the Yeba formation, southern gangdese, south Tibet. *Int. Geol. Rev.* 50 (5), 442–471. doi:10.2747/0020-6814.50.5.442

Zhu, D., Wang, Q., Cawood, P. A., Zhao, Z., and Mo, X. (2017). Raising the gangdese mountains in southern Tibet. *J. Geophys. Res. Solid Earth* 122 (1), 214–223. doi:10.1002/2016JB013508

Zhu, D., Wang, Q., Chung, S., Cawood, P., and Zhao, Z. (2018). *Gangdese magmatism in southern Tibet and India–asia convergence since 120 Ma*. 483. London: Geological Society of London 483, 583–604. doi:10.1144/SP483.14

Zhu, D., Wang, Q., Weinberg, R. F., Cawood, P. A., Zhao, Z., Hou, Z., et al. (2023). Continental crustal growth processes recorded in the gangdese batholith, southern Tibet. *Annu. Rev. Earth Planet. Sci.* 51 (51), 155–188. doi:10.1146/annurev-earth-032320-110452

Zhu, D., Zhao, Z., Niu, Y., Dilek, Y., Hou, Z., and Mo, X. (2013). The origin and pre-Cenozoic evolution of the Tibetan Plateau. *Gondwana Res.* 23 (4), 1429–1454. doi:10.1016/j.gr.2012.02.002

Zhu, D., Zhao, Z., Niu, Y., Mo, X., Chung, S., Hou, Z., et al. (2011). The Lhasa Terrane: record of a microcontinent and its histories of drift and growth. *Earth Planet. Sci. Lett.* 301 (1), 241–255. doi:10.1016/j.epsl.2010.11.005

Zhu, D., Zhao, Z., Pan, G., Lee, H., Kang, Z., Liao, Z., et al. (2009). Early cretaceous subduction-related adakite-like rocks of the Gangdese Belt, southern Tibet: products of slab melting and subsequent melt–peridotite interaction? *J. Asian Earth Sci.* 34 (3), 298–309. doi:10.1016/j.jseaes.2008.05.003